Chinese Chemical Letters 37 (2026) 112556

Contents lists available at ScienceDirect

Chinese Chemical Letters

journal homepage: www.elsevier.com/locate/cclet

Structural engineering of piezocatalysts for piezo-driven H_2O_2 production: Enabling multifunctional integration in advanced wastewater remediation

Yue Yin[a,b], Yaping Fan[a,b], Jiao Yang[a,b,*], Yi Ren[c,*], Bo Lai[d]

[a] School of Ecology and Environment, Zhengzhou University, Zhengzhou 450001, China
[b] Henan International Joint Laboratory of Environment and Resources, Zhengzhou 450001, China
[c] State Key Laboratory of Hydraulics and Mountain River Engineering, College of Water Resource & Hydropower, Sichuan University, Chengdu 610065, China
[d] State Key Laboratory of Hydraulics and Mountain River Engineering, College of Architecture and Environment, Sichuan University, Chengdu 610065, China

ARTICLE INFO

Article history:
Received 4 July 2025
Revised 6 February 2026
Accepted 26 February 2026
Available online 27 February 2026

Keywords:
Piezocatalysis
H_2O production
Structure-function relationships
Structural engineering
Wastewater remediation

ABSTRACT

Piezocatalysis based on electrode polarization processes represents a highly promising approach for *in-situ* H_2O_2 generation. The efficiency of piezocatalytic H_2O_2 generation faces dual constraints from extrinsic operational parameters like excitation frequency and intrinsic material properties, particularly crystallographic characteristics and polarization magnitude governing charge separation kinetics. Consequently, structural optimization targeting enhanced polarization response, accelerated charge transfer, and strengthened reactant adsorption at active sites has become a central research imperative. This review evaluates piezoelectric material design strategies, establishes structure-function relationships spanning multiscale features and H_2O_2 production efficiency, and assesses technological viability for advanced wastewater remediation. By systematically analyzing core structural determinants, including crystal symmetry, heterojunction, surface functionalization, polymerization degree, and microstructural parameters (porosity/thickness), across diverse piezocatalytic systems, we elucidate governing structure-function interdependencies for H_2O_2 production. These determinants have been further validated in material classes spanning perovskites, bismuth-based layered compounds, wurtzite-type materials, transition metal dichalcogenides, carbon-based materials, polymers, metal-organic frameworks, and MAX phase materials. These insights will establish mechanistic foundations for *in-situ* H_2O_2 synthesis, advancing sustainable water remediation *via* piezocatalysis.

© 2026 Published by Elsevier B.V. on behalf of Chinese Chemical Society and Institute of Materia Medica, Chinese Academy of Medical Sciences.

1. Introduction

Hydrogen peroxide (H_2O_2), a carbon-free energy carrier with a high volumetric energy density (5.0×10^6 J/L) [1], has been widely applied in fields such as wastewater treatment [2–4], medical disinfection [5], and chemical synthesis [6–8]. Global H_2O_2 production currently exceeds 4 million tons annually, but its transportation and storage incur significant safety risks [7–9]. Storage-induced autodecomposition further elevates operational costs [10]. Consequently, efficient and environmentally friendly technologies for the *in-situ* H_2O_2 generation have become a prominent research focus in recent years [11–13].

Piezocatalysis offers a transformative alternative to the energy-intensive anthraquinone process by enabling mild *in-situ* H_2O_2 generation under ambient conditions, achieving higher turnover frequency through superior electron utilization while eliminating high-pressure reactors and toxic solvents inherent to conventional methods [14]. Pierre *et al.* first observed pressure-dependent surface charge generation on quartz and tourmaline crystals, noting proportional charge accumulation under mechanical stress and immediate dissipation upon stress removal [15]. This phenomenon, where mechanical deformation induces relative displacement of positive/negative charge centers, generating polarized surface charges and establishing potential gradients, is termed the piezoelectric effect [16]. Recently, piezocatalysis has rapidly advanced by harvesting ambient mechanical energy (*e.g.*, vibrations, hydraulic forces) to activate piezoelectric polarization fields, thereby releasing free charges (electrons/holes) that drive redox reactions [17]. This environmentally compatible strategy circumvents storage-induced autodecomposition through on-site production, empowering critical energy-environment applications including

* Corresponding authors.
E-mail addresses: jiaoyang@zzu.edu.cn (J. Yang), yren@scu.edu.cn (Y. Ren).

https://doi.org/10.1016/j.cclet.2026.112556
1001-8417/© 2026 Published by Elsevier B.V. on behalf of Chinese Chemical Society and Institute of Materia Medica, Chinese Academy of Medical Sciences.

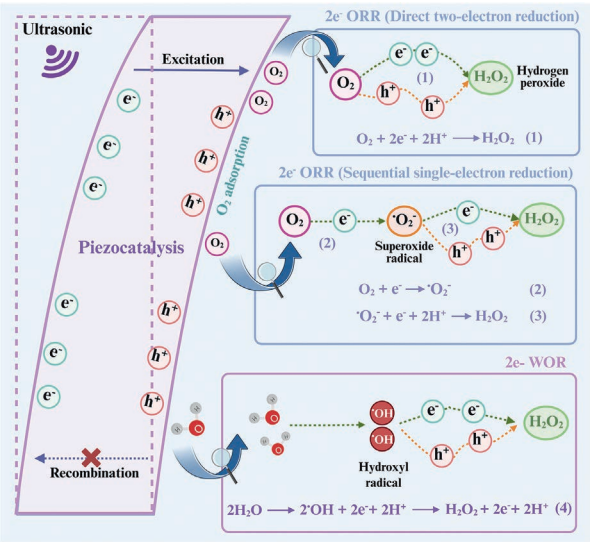


Fig. 1. Schematic of the ORR and WOR piezoelectric process.

CO_2 reduction [18], water splitting for H_2 evolution [19], and H_2O_2 synthesis [20].

The piezoelectric effect originates from mechanical stress-induced lattice deformation, displacing internal charge centers to generate polarized electric fields [21–23]. Structural anisotropy enables external forces to misalign cation/anion positions, creating dipole moments whose magnitude governs piezoelectric potential strength. Higher polarization intensity yields stronger built-in electric fields that enhance catalytic kinetics [24]. Crucially quantified by the piezoelectric coefficient (d_{33}), Pb(Zr, Ti)O_3 exhibits superior charge generation efficiency (400 pC/N) *versus* $BaTiO_3$ (100 pC/N), necessitating greater mechanical energy input for equivalent catalytic efficacy in the latter [25]. Polarization magnitude further correlates with crystal symmetry (*e.g.*, non-centrosymmetric $BiFeO_3$ below Curie temperature), defect density (oxygen vacancy-optimized $BiFeO_3$ achieves 110.07 μmol g^{-1} h^{-1} H_2O_2) [26], and morphology, where nanostructures amplify responses *via* elevated surface-area-to-volume ratios and stress concentration [27]. Morphological control is evidenced by ultrathin ZnO/Al_2O_3 (4.5 nm) exhibiting higher surface potential (1.42 V) than ZnAl-LDH (1.23 V) [28], and $BaTiO_3$ nanowires generating 56-fold greater piezopotential (11.2 V *vs.* 0.2 V) than nanoparticles under identical stress [29]. These findings demonstrate that multiscale structural engineering plays a decisive role in governing piezoelectric properties.

Through precision engineering of material structure, including crystal structure, microarchitecture, defect configurations, and surface characteristics, the built-in electric fields can be intensified and polarization responses optimized. This synergistic enhancement directly elevates piezocatalytic H_2O_2 generation efficiency. This study focuses on structure-property relationships governing piezoelectric responses across key material classes, correlating structural descriptors with mechano-catalytic performance. And we further interrogate their application in mechano-driven H_2O_2 production for advanced wastewater remediation, with critical emphasis on strain-mediated surface charge redistribution mechanisms that steer oxygen reduction reaction (ORR) and water oxidation reaction (WOR) (Fig. 1). By establishing polarized field-driven piezo-catalytic synergy mechanisms, this work advances functional material design for sustainable H_2O_2 production and *in-situ* water remediation technologies.

2. Correlation between piezocatalyst structure and H_2O_2 production

2.1. Impact of catalyst structure on piezocatalytic H_2O_2 production

In piezocatalytic systems, H_2O_2 generation is governed by synergistic interactions between extrinsic operational parameters and intrinsic material properties. As the core determinant, multiscale structural characteristics of piezocatalysts constitute the primary focus of this review. We establish foundational correlations between catalyst architecture and H_2O_2 production performance, specifically examining how interfacial, crystalline, and macroscopic properties dictate functional outcomes. Consequently, elucidating fundamental structure-function relationships, while evaluating practical viability for catalytic H_2O_2 synthesis, emerges as a critical imperative. This section thereby provides the framework for developing high-activity piezocatalysts and designing targeted modification strategies. Detailed analyses of extrinsic parameters including ultrasonic frequency/power, pH, and temperature are comprehensively addressed in Supporting information.

2.1.1. Crystal structure

The crystal structure intrinsically dictates piezoelectric properties, charge separation efficiency, and surface reactivity of materials, directly controlling H_2O_2 production yield and selectivity [30]. Piezoelectric effects exclusively arise in acentric crystal structures. Of the 32 crystallographic point groups, 20 exhibit piezoelectricity due to asymmetric configurations that enable effective charge separation. Crystallographic symmetry critically governs piezoelectric polarization capability and built-in electric field strength, thereby regulating H_2O_2 generation performance [31]. Therefore, modulating crystallographic symmetry consequently offers a promising approach for enhancing piezoelectric functionality.

Elemental doping induces significant lattice distortion and enhances structural asymmetry in piezoelectric materials, offering an effective strategy for performance enhancement. Li *et al.* synthesized V-doped $NaNbO_3$ where V-O bond lengths (3.29 Å) closely matched Nb-O lengths (3.33 Å), preserving structural integrity while the slight contraction amplified asymmetry [32]. This yielded enhanced piezoelectric activity, with 10 % V-doped $NaNbO_3$ achieving 102.6 μmol g^{-1} h^{-1} H_2O_2 production, which 2.2-fold higher than pristine material. Although hexagonal boron nitride (h-BN) possesses intrinsic Lewis acid-base sites for adsorbing O_2, H_2O, and intermediates, its wide bandgap (5.0–6.0 eV) impedes carrier generation and migration. Moreover, the centrosymmetric structure of bulk h-BN typically suppresses piezocatalytic effects (Fig. 2a) [33]. Ni *et al.* addressed this through carbon doping, which reduced the valence band maximum from −5.85 eV (h-BN) to −2.65 eV carbon-doped h-BN (h-BCN) [34]. Carbon atoms induced asymmetric electron distribution in h-BCN nanosheets (~140 nm thickness), activating bulk piezocatalytic behavior. Elemental doping simultaneously expands lattice asymmetry through structural distortion and lattice mismatch, while enabling central-site ion substitution that triggers dipole displacement. This synergy enhances piezoelectric polarization, demonstrating that optimized doping levels can strategically boost piezocatalytic activity.

Vacancy engineering further disrupts lattice symmetry, enhances local polarity, and amplifies piezoelectric responses [35]. Oxygen vacancies (OVs) with enriched localized electrons serve as active sites that modulate charge density distribution, thereby reducing the energy barrier for oxygen reduction through enhanced O_2 adsorption and activation [36]. These highly reactive OVs play pivotal roles in catalysis. However, excessive OVs concentrations impair electron transfer efficiency, diminishing H_2O_2 yields. While OVs in $BaTiO_3$ enhance piezocatalytic activity, a volcanic trend

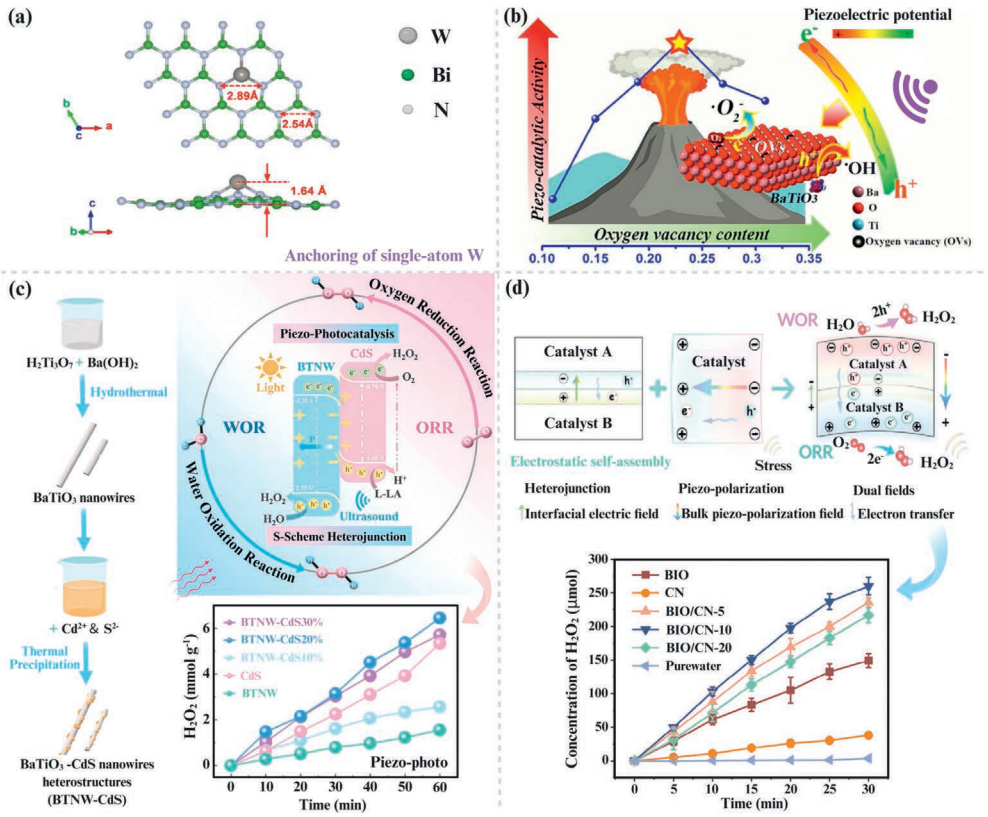


Fig. 2. The influence of (a) crystal structure, (b) oxygen vacancies, and (c, d) heterojunction on the production of H_2O_2 by piezoelectricity. (a) Reproduced with permission [33]. Copyright 2022, Elsevier. (b) Reproduced with permission [37]. Copyright 2020, Elsevier. (c) Reproduced with permission [42]. Copyright 2025, Elsevier. (d) Reproduced with permission [43]. Copyright 2024, Wiley.

emerges where activity peaks then declines with increasing OVs density (Fig. 2b) [37]. Thus, optimal OVs concentrations must simultaneously provide sufficient O_2 adsorption sites and maintain efficient electron transport pathways. Cai *et al.* synthesized ultrathin $Bi_4O_5Br_2$ nanosheets (~5 nm) with tunable OVs concentrations by modulating water/ethylene glycol ratios [38] The synergy between OVs and nanoscale thickness enhanced piezoelectric properties while facilitating charge separation. DFT calculations confirmed OVs significantly improve O_2 adsorption/activation and reduce ΔG barriers in reaction pathways. The OV-optimized nanosheets achieved an exceptional H_2O_2 production rate of 2700 μmol g^{-1} h^{-1} in pure water, predominantly *via* the 2e⁻-ORR pathway. Moreover, vacancy introduction modulates reaction selectivity. Zeng *et al.* demonstrated that OVs in $BiFeO_3$ elevate the valence band position, which thermodynamically favors enhanced oxidative capacity and selectively promotes the WOR pathway [26].

Although doping and vacancy engineering enable band structure modulation, excessive incorporation compromises lattice stability [39]. Critically, the quantitative correlation between asymmetric structural modulation and piezoelectric performance remains elusive, with predictive theoretical models for optimal design still lacking. Consequently, integrating machine learning with *in-situ* characterization techniques becomes essential to optimize materials. This includes exploring multi-field coupling effects (*e.g.*, opto-electro-mechanical synergy) and probing unique piezoelectric behaviors in low-dimensional structures such as nanowires and quantum dots, thereby enhancing H_2O_2 production while ensuring structural sustainability.

2.1.2. Heterojunction

The rapid recombination of electron-hole pairs represents a primary constraint on piezocatalytic efficiency. At heterojunction interfaces, differential band structures, electron affinities, or work functions generate built-in electric fields and band bending that facilitate directional charge transfer, effectively suppressing carrier recombination [40]. Consequently, constructing heterojunctions through coupling piezoelectric materials with semiconductors provides a promising strategy to mitigate this limitation [41].

In piezocatalysis, heterojunctions optimize piezocatalytic charge separation and surface reaction kinetics through interface-induced electric fields (Figs. 2c and d) [42,43]. Zhou *et al.* engineered a $BiOI/BiVO_4$ p-n heterojunction featuring an asymmetric interface with a built-in electric field [44]. The piezoresponse of this p-n heterojunction is primarily governed by ultrasonically induced polarization intensity, with further enhancement mediated through the built-in electric field. Ultrasonically enhanced polarization coupled with interfacial fields elevated H_2O_2 production to 480 μmol g^{-1} h^{-1}, surpassing individual $BiVO_4$ and BiOI by 1.6-fold and 12-fold, respectively. Besides, integrating piezocatalysis with photocatalysis provides another effective approach to suppress charge recombination. For instance, Pham *et al.* constructed an S-scheme heterojunction by compositing g-C_3N_4 with CdS, addressing the rapid electron recombination in pristine g-C_3N_4 [45]. The heterostructure attained a H_2O_2 yield of 23.44 μmol g^{-1} h^{-1}, exceeding the performance of its individual constituents, 11.66 μmol g^{-1} h^{-1} for g-C_3N_4 and 19.89 μmol g^{-1} h^{-1} for CdS.

Heterojunctions significantly enhance piezocatalytic performance through interfacial engineering, offering distinct advantages. The built-in electric field effectively suppresses electron-hole recombination and improves charge separation efficiency, thereby boosting piezocatalytic activity [46,47]. However, structural characteristics such as heterojunction thickness may compromise piezoelectric response and substrate accessibility. Consequently, balancing the trade-off relationship between these structural features and

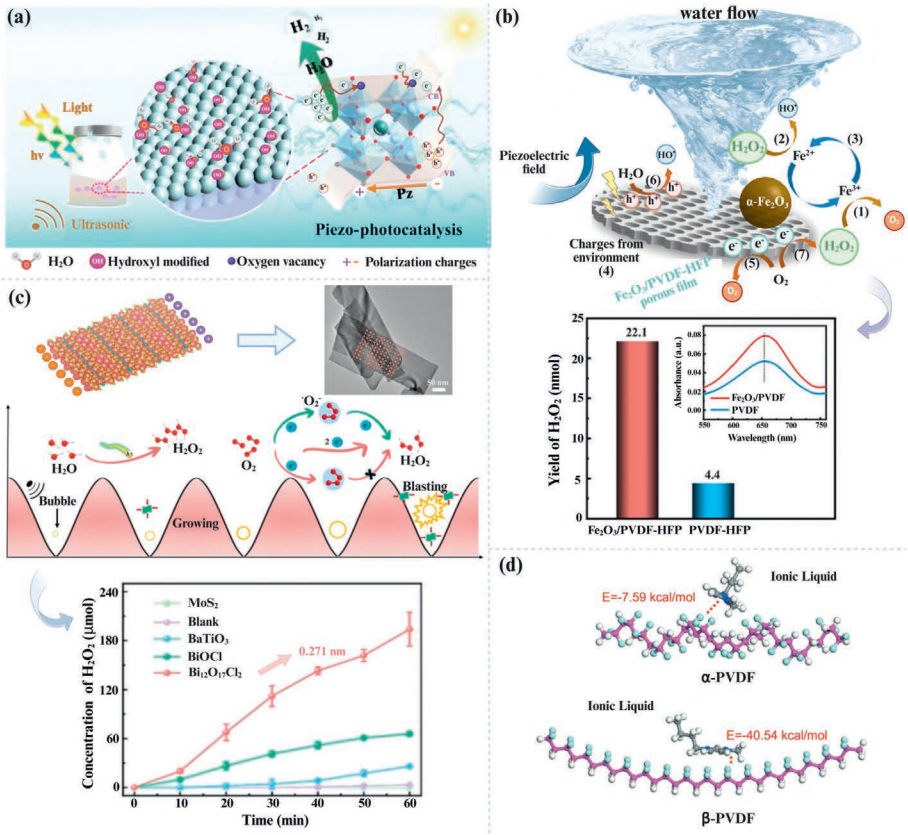


Fig. 3. The influence of (a) surface functional groups, (b) pores, (c) thickness and (d) degree of polymerization on the production of H_2O_2 by piezoelectricity. (a) Reproduced with permission [53]. Copyright 2022, Elsevier. (b) Reproduced with permission [59]. Copyright 2022, Elsevier. (c) Reproduced with permission [70]. Copyright 2024, Wiley. (d) Reproduced with permission [71]. Copyright 2024, Wiley.

piezocatalytic efficiency remains an imperative challenge for optimizing heterojunction structures.

2.1.3. Surface functional groups

Surface functional groups critically govern piezocatalytic H_2O_2 production by modulating active sites, activating reactants, and enhancing polarization [48–50]. Zhou *et al.* validated this principle using carbon-functionalized BiOCl nanosheets [51]. By selectively deactivating C=O, -OH, and -COOH groups with phenylhydrazine, benzoic anhydride, and 2–bromo-1-phenylethanone blocking agents, they demonstrated that suppressing -OH functionality reduced H_2O_2 yield to levels approaching unmodified BiOCl. This confirmed -OH groups as primary active sites for O_2 activation, while C=O and -COOH deactivation showed negligible impact. Notably, water adsorption-desorption processes share these same active sites. Further mechanistic insights arise from Zhang *et al.*, who employed H_2O-TPD to probe water-catalyst interactions [52]. Ag/BNT-AN exposed enhanced active sites for water adsorption/activation, with reduced surface -OH density indicating improved water oxidation capacity. Complementarily, Jiang *et al.* synthesized -OH modified $SrTiO_3$ exhibiting dual functionalities, which surface-attached -OH groups improve hydrophilicity to expose more active sites for water dissociation, while simultaneously generating OVs that trap electrons to facilitate directional charge transfer and suppress recombination (Fig. 3a) [53]. Collectively, these studies suggest that optimal surface -OH density critically balances hydrophilicity, active site accessibility, and piezoelectric charge separation efficiency.

The integration of polar halogen functional groups substantially enhances piezoelectric properties. Chen *et al.* demonstrated that incorporating highly electronegative fluorine groups (-F) into polymers intensifies piezoelectric responses, where stronger electronegativity correlates directly with amplified built-in electric fields in polymer fibers [54]. Similarly, Wang *et al.* engineered self-assembled monolayers (SAMs) on Ti_3C_2 surfaces to improve environmental stability and piezocatalytic activity [55]. Surface-modified Ti_3C_2 exhibited altered lattice parameters and symmetry, consequently increasing polarization. Polar SAMs functional groups significantly elevated Ti_3C_2 surface potential, facilitating piezoelectric electron migration. The Ti_3C_2/SAMs-NH_2 configuration achieved optimal performance with 7-fold enhanced BPA degradation efficiency. Halogen functionalities further suppress charge recombination through polarization effects. Electronegative groups such as -Cl induce interfacial polarization upon surface modification, prolonging charge carrier lifetimes. Liu *et al.* validated this mechanism using Cl-intercalated $BiVO_4$, where Cl-Bi bonding distorts BiO_6 octahedra [56]. This distortion amplifies structural acentricity under mechanical stress, strengthening intrinsic piezoelectric polarization and piezoresponse.

Furthermore, surface functional group introduction disrupts intrinsic crystallographic symmetry through non-centrosymmetric chemical bonding configurations, inducing lattice distortion and symmetry breaking [57]. These microstructural modifications substantially enhance piezoelectric performance through synergistic mechanisms. Symmetry reduction establishes the fundamental prerequisite for piezoelectric phenomena. And polarization effects from functional groups amplify intrinsic electric dipole moments, elevating piezoelectric coefficients [58]. Therefore, developing piezoelectric materials with tunable polar groups while establishing quantitative models for surface-group-mediated charge shielding and band structure modulation becomes essen-

tial for guiding material optimization and predicting catalytic performance.

2.1.4. Pores

Optimally interconnected pores facilitate rapid diffusion of reactants (O_2, H_2O) to active sites while enabling efficient H_2O_2 desorption, thereby mitigating local concentration polarization (Fig. 3b) [59]. Hierarchical pore structures synergistically enhance mass transfer through distinct functionalities: Micropores provide high specific surface area, mesopores stabilize intermediate adsorption, while macropores enable rapid molecular transport. Furthermore, pore edges inherently concentrate lattice defects such as oxygen vacancies, which act as electron-trapping centers that promote piezoelectric charge separation and enhance production efficiency for reactive oxygen species (ROS) including $^{\bullet}OH$ and $^{\bullet}O_2^-$ [60,61].

Elevated porosity substantially increases the specific surface area of materials, exposing more piezoelectric active sites and thereby enhancing H_2O_2 production rates [62]. Garcia *et al.* fabricated porous ZnO thin films *via* oblique-angle deposition, achieving a porosity of 9.6 % with a piezoelectric coefficient of 115.6 pC/N, which significantly higher than the 11.6 pC/N observed in non-porous ZnO [63]. Hierarchical pore structures similarly optimize catalytic H_2O_2 production. Thomas *et al.* engineered a hierarchical covalent organic framework (macro-TpBpy) wherein micropores maximize surface area while macropores facilitate substrate transport [64]. This optimized architecture elevated H_2O_2 yield to 2716 μmol g^{-1} h^{-1} (27 % higher than pristine TpBpy) while effectively suppressing side reactions from localized charge accumulation.

Maximizing specific surface area while preserving mechanical stability necessitates precise pore density regulation. Hierarchical pore systems further optimize catalytic efficiency by synergistically matching mass transfer with reaction kinetics. Surface chemical modifications, through doping or functional group incorporation, additionally fine-tune pore surface hydrophilicity/hydrophobicity. This optimizes H_2O/O_2 adsorption equilibria, critically enhancing catalytic selectivity and operational stability.

2.1.5. Thickness

Lamellar nanomaterials exhibit superior piezoresponse and catalytic activity due to enlarged specific surface areas and amplified stress concentration effects. Thickness modulation optimizes catalytic pathways by tuning bandgap, carrier concentration, and piezoelectric coefficients [65]. Gao *et al.* demonstrated $BaTiO_3$ nanosheets achieve 521 μmol g^{-1} h^{-1} H_2O_2 production, surpassing particulate $BaTiO_3$ (167 μmol g^{-1} h^{-1}) by 3.1-fold [66]. Similarly, in $SrBi_2Ta_2O_9$ lamellae, predominant (001) plane exposure enhances *c*-axis polarization, creating internal electric fields that directionally separate carriers while reduced thickness shortens migration paths to suppress recombination [67]. Ultrathin $SrBi_2Ta_2O_9$ maximizes ultrasonic deformation susceptibility and charge asymmetry, intensifying piezoelectric fields for efficient redox reactions. Moreover, Wang *et al.* synthesized sub-50 nm MoS_2@MWCNTs nanoflower-tubular hybrids (<6 nm ultrathin regions) exhibiting 94.4 mV piezoresponse, which was 4.07-fold higher than bulk MoS_2 [68]. Thickness reduction amplifies interlayer polarization, generates stronger built-in fields for charge separation, and expands interlayer spacing to enhance H_2O/O_2 diffusion and confined-space activation [69]. Comparative studies reveal $Bi_{12}O_{17}Cl_2$ lamellae (∼0.95 nm) achieve about 3-fold higher H_2O_2 production than BiOCl (3.4 nm) due to superior mechanical deformation efficiency (Fig. 3c) [70].

Advancing research confirms that material thickness modulates piezoelectric effects through three fundamental mechanisms: Increased surface area, stress sensitivity, and crystallographic polarization. Ultrathin structures enhance carrier separation efficiency, reactant diffusion kinetics, and piezo-electronic coupling *via* intensified mechanical deformation. Emerging thickness-control techniques and emergent 2D heterostructures promise enhanced dynamic responsiveness and operational stability, extending piezocatalytic applications to environmental remediation, energy conversion, and biomedical engineering. Through multiscale structural design and mechanistic innovation, piezocatalysis may pioneer new pathways for green chemistry and sustainable energy technologies.

2.1.6. Degree of polymerization

The degree of polymerization (DP) primarily influences piezoelectric properties indirectly through its effects on crystallization behavior, chain segment mobility, and processability, rather than directly determining piezoelectric coefficients (*e.g.*, d_{33}). Compared to crystallinity, molecular polarity, and compositing strategies, DP optimization remains secondary. For polyvinylidene difluoride (PVDF), piezoelectric enhancement relies more critically on β-phase content (achieved through stretching or annealing) than on DP elevation alone (Fig. 3d) [71]. The β-phase adopts an all-trans conformation with highly ordered molecular chain alignment, enabling significant electric dipole moment variations under mechanical stress [72]. While higher DP may promote ordered packing that increases β-phase content, excessive DP induces chain entanglement that impedes crystallization [73]. Thus, DP must balance "sufficient length for structural ordering" against "excessive entanglement avoidance". Furthermore, polymer piezoelectric require molecular chain orientation *via* stretching or electric poling to enhance cooperative dipole alignment. Longer chains (higher DP) may facilitate highly oriented structures during stretching, but excessively high DP increases material brittleness, compromising processability [74]. This stems partly from DP's impact on copolymer segment distribution homogeneity or filler dispersion. Ultimately, DP must exceed a critical threshold to enable ordered structure formation, but its influence plateaus beyond this threshold due to asymptotic saturation effects.

In PVDF film research, DP typically adheres to industry standards, with emphasis placed on β-phase induction and poling methodologies. Functioning as an indirect modulator, DP necessitates synergistic calibration with primary performance determinants, notably crystallinity control and poling processes. Consequently, material design prioritizes crystallization kinetics, molecular polarization alignment, and composite formulation strategies, whereas DP selection primarily addresses processing feasibility and mechanical robustness.

2.2. Correlation between catalyst types and piezocatalytic H_2O_2 generation performance

Building upon the aforementioned structural characteristics, this section systematically summarizes piezoelectric catalytic H_2O_2 production across diverse material systems, including perovskites, bismuth-based layered compounds, wurtzite-type materials, transition metal dichalcogenides (TMDCs), carbon-based materials, polymers, metal-organic frameworks (MOFs), and MAX phase materials. And the performance variations in piezocatalytic H_2O_2 production across distinct catalyst systems are listed in Table S1 (Supporting information).

2.2.1. Perovskite

Perovskite oxide materials, composed of metal cations and oxygen anions, adopt the general formula ABO_3 with a cubic symmetric crystal structure as the fundamental unit [75]. The perovskite framework accommodates diverse cationic dopants,

enabling symmetry modification for enhanced piezoelectric properties [76]. $ATiO_3$-type perovskites, including $PbTiO_3$ [77], $BaTiO_3$ [78], and $SrTiO_3$ [79], are widely employed in piezocatalysis. In $BaTiO_3$, Ti atoms occupy octahedral centers coordinated by six O atoms, while Ba resides at unit cell corners. Polarization arises from relative displacements between Ti^{4+} and O^{2-}, with non-centrosymmetric tetragonal $BaTiO_3$ exhibiting substantially higher polarization along the [001] direction than its cubic phase.

Significant compositional flexibility at A/B sites permits tailored modifications of crystal structure, redox activity, and oxygen vacancy concentration through metal ion substitution [80,81]. Controlled doping fine-tunes piezoelectric coefficients within specific ranges, offering critical advantages for piezocatalytic applications. Hou *et al*. synthesized double-perovskite piezocatalysts $Ba_2Nb_{2-x}Fe_xO_6$. In $Ba_2Nb_{2-x}Fe_xO_6$, Fe incorporation breaks cubic symmetry to promote tetragonal phase evolution, generating intrinsic piezoelectricity, while simultaneously modulating physicochemical properties by narrowing bandgap, enhancing electronic conductivity, and increasing charge carrier density and defect concentration. This synergy enables dual-pathway H_2O_2 generation *via* WOR and ORR under O_2-saturated conditions, achieving 690 μmol g^{-1} h^{-1} yield.

Morphological engineering also effectively optimizes piezoelectric performance in perovskites. Conventionally structured (K, Na)NbO_3 exhibits limited piezocatalytic activity due to sparse active sites. To address this, Wang *et al*. implemented a morphology-control approach utilizing high-energy pendulum ball milling instead of conventional ball milling to deliberately create uneven raw material distribution, synthesizing (K, Na)NbO_3 catalysts with stepped-surface morphology [82]. This configuration enhances edge exposure and active site density, significantly boosting piezocatalytic activity. While larger particles exhibit diminished quantum size effects, their dispersibility optimizes piezoelectric utilization, enabling exceptional micron-scale catalytic performance. Gao *et al*. reported piezocatalytic H_2O_2 production rates of 167, 521, and 1088 μmol g^{-1} h^{-1} for $BaTiO_3$ powder, single-crystal nanosheets, and Ag-decorated nanosheets, respectively (Fig. 4a) [66]. The enhanced performance of Ag-decorated systems stems from interfacial electron enrichment at metal-semiconductor junctions. This phenomenon strengthens O_2 adsorption, increases catalytic active sites, and boosts $^{\bullet}O_2^-$ generation, ultimately accelerating H_2O_2 production kinetics.

Surface modification also holds significant importance for enhancing piezocatalytic performance. Zhang *et al*. strategically integrated piezoelectric enhancement and surface engineering to optimize piezocatalytic H_2O_2 production over $Bi_{0.5}Na_{0.5}TiO_3$ (BNT) [52]. Their approach produced Ag-decorated $Bi_{0.5}Na_{0.5}TiO_3$-$AgNbO_3$ solid solution (Ag/BNT-AN), a highly stable catalyst for dual-pathway H_2O_2 generation. Concurrent piezoelectric improvement *via* Ag/BNT-AN co-substitution and synergistic ORR/WOR promotion through Ag nanomaterials with hydroxyl surface modification substantially amplified piezocatalytic activity. Under ultrasonication, Ag/BNT-AN achieved an H_2O_2 production rate of 469 μmol g^{-1} h^{-1}, representing a 13-fold increase over pristine BNT.

Enhancement strategies for perovskite piezocatalysts center on synergistic compositional engineering and morphological control. Specifically, strategic adjustment of A/B-site elements and dopants optimizes crystallographic symmetry and piezoelectric coefficients, thereby amplifying mechanical stress-induced charge polarization. Moreover, directional synthesis of nanoflakes or nanowires shortens charge migration pathways while exposing abundant active sites through high specific surface areas. Complementarily, composite fabrication exploits low-energy charge-transfer barriers at interfaces to facilitate electron-hole separation, with interfacial piezoelectronic coupling further enhancing localized charge density.

2.2.2. Bismuth-based layered compounds

Bismuth-based layered materials, including BiOX (X = I, Br, Cl), $Bi_4O_4Br_2$, Bi_2WO_6, $BiOClO_3$, $Bi_{12}O_{15}Cl_6$, constitute a prominent class of piezoelectric materials [83]. These crystals feature an ordered layered structure formed by the alternating stacking of tetragonal $(Bi_2O_2)^{2+}$ layers with halide ions, perovskite-like $(A_{n-1}B_nO_{3n+1})$ slabs, or intercalated ions (*e.g.*, CO_3^{2-}, BO_3^{3-}, NO_3^-) along the *c*-axis (Figs. 4b and c) [51,84]. Ionic groups or interlayer ions reside at the central positions between adjacent $(Bi_2O_2)^{2+}$ layers.

This structural ordering enables efficient internal electric field generation under mechanical stress, facilitating effective charge separation [85]. Wang *et al*. synthesized ultrathin $Bi_4Ti_3O_{12}$, which exhibits a strong piezoelectric response due to the off-center displacement of Ti^{4+} ions within TiO_6 octahedral units [83]. This piezoelectric response intensifies with diminishing thickness, as evidenced by a d_{33} of 183.43 pm/V and H_2O_2 production rate of 161.12 μmol g^{-1} h^{-1} for 4.2-nm-thick nanosheets, while 25.8-nm-thick counterparts show reduced values of 69.75 pm/V and 86.48 μmol g^{-1} h^{-1}. Separately, Cai *et al*. reported efficient piezocatalytic H_2O_2 generation in pure water using ultrathin $Bi_4O_5Br_2$ nanosheets (~5 nm) [38]. The ultrathin nanostructure simultaneously enhances piezoelectric polarization and promotes stress-driven charge separation. Concurrently, oxygen vacancies at nanosheet edges improve O_2 adsorption/activation and significantly reduce the ΔG barrier for reaction pathways, achieving an exceptional H_2O_2 yield of 620 μmol g^{-1} h^{-1}.

The inherent polarization of bismuth-based layered compounds enables efficient charge carrier separation under mechanical stress through their two-dimensional architecture. Moreover, ultrathin configurations expose abundant active sites, while strategically introduced oxygen vacancies significantly enhance piezocatalytic H_2O_2 generation performance.

2.2.3. Wurtzite-type materials

Wurtzite-type structures crystallize in a hexagonal system where anions (*e.g.*, S^{2-}, O^{2-}) adopt a hexagonal close-packed (hcp) arrangement, with cations (*e.g.*, Zn^{2+}) occupying tetrahedral interstices within the anion sublattice (Fig. 4d) [86]. At ambient conditions, ZnO adopts the hexagonal wurtzite structure (space group $P6_3mc$), belonging to the 6 mm point group. Each Zn^{2+} ion resides in tetrahedral coordination with O^{2-} ions, forming Zn-O_4 tetrahedra. This non-centrosymmetric structure enables mechanical stress to displace Zn^{2+} cations relative to O^{2-} anions, disrupting charge equilibrium and generating dipole realignment. Consequently, spontaneous polarization develops along the *c*-axis [87].

Bulk ZnO exhibits a d_{33} of 9.9 pm/V, while studies confirm that reduced crystal dimensions significantly enhance d_{33} [88]. For instance, *c*-axis-oriented ZnO films achieve $d_{33} = 12.5$ pm/V at 1 μm thickness, whereas 60-nm-thick ZnO nanoribbons exceed 25 pm/V [89]. Mahmood *et al*. synthesized large-area, nanometer-thick ZnO sheets *via* a liquid-metal-based approach [90]. These ultrathin ZnO sheets (hundreds of micrometers wide) maintain stable crystallinity and hexagonal phase purity, with 1.1-nm-thick samples reaching $d_{33} = 80$ pm/V, approximately 8-fold higher than bulk ZnO. Similarly, Nie *et al*. fabricated 4.5-nm-thick ZnO/Al_2O_3 composites by calcining Zn-Al LDH precursors [28]. The ultrathin composites demonstrate enhanced piezopotentials through facile bending deformation. Supporting this observation, COMSOL finite element simulations reveal lateral surface potential differences reaching 1.42 V for 5-nm ZnO models compared with 1.23 V for 20-nm structures under equivalent deformation, corroborating superior piezoelectric induction in thinner structure.

Furthermore, metal doping significantly enhances piezoelectric coefficients in zinc oxide by modifying crystallographic symmetry. Pan *et al*. synthesized high-piezoelectric-coefficient ZnO

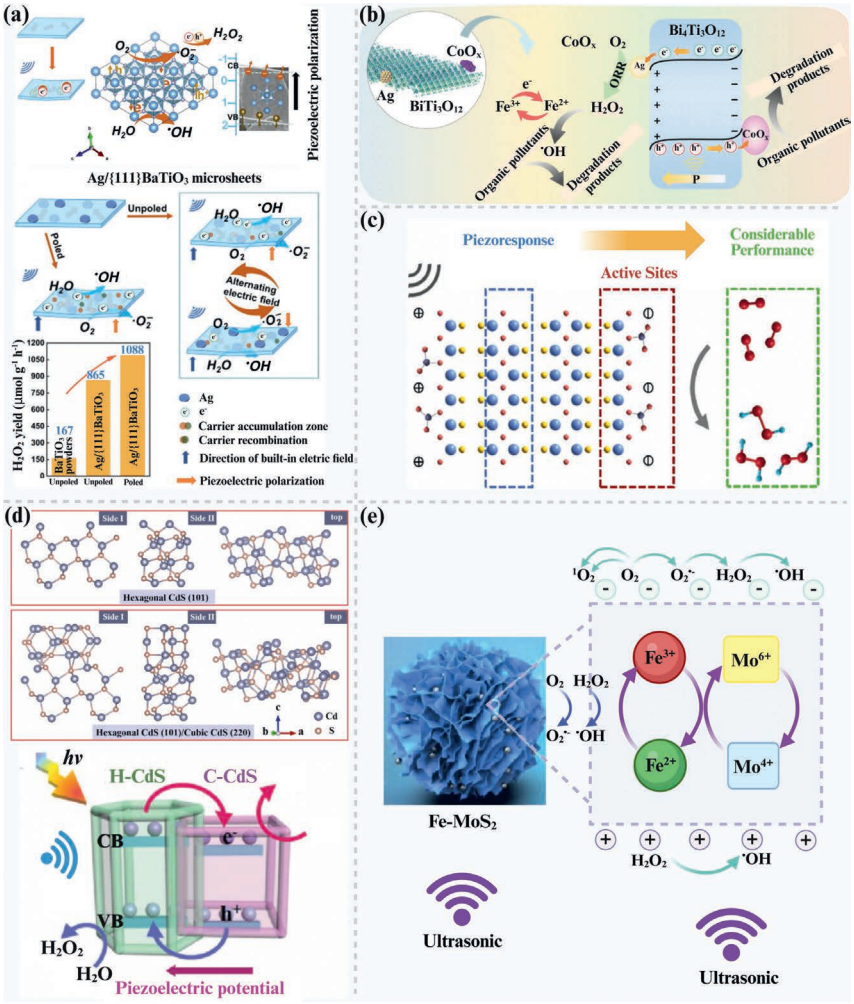


Fig. 4. Piezoelectric catalytic H_2O_2 production in (a) ABO_3-type perovskite, (b, c) bismuth-based layered compounds, (d) wurtzite-type materials, and (e) TMDCs systems. (a) Reproduced with permission [66]. Copyright 2025, Elsevier. (b) Reproduced with permission [84]. Copyright 2025, RSC. (c) Reproduced with permission [51]. Copyright 2024, Elsevier. (d) Reproduced with permission [86]. Copyright 2021, Elsevier. (e) Reproduced with permission [105]. Copyright 2025, Elsevier.

doped with Fe^{3+} ($d_{33} = 127$ pm/V), Cr^{3+} ($d_{33} = 120$ pm/V), and V^{5+} ($d_{33} = 110$ pm/V) [91–93]. Similarly, Chen *et al.* fabricated MgxZn$_{1-x}$O thin films *via* Mg^{2+} doping, achieving a d_{33} value of 54.1 pm/V [94], and Sinha *et al.* documented d_{33} values of 30, 43, 45, and 101 pm/V for Ce^{3+}-, Eu^{3+}-, Gd^{3+}-, and La^{3+}-doped ZnO nanorods, respectively [95–97]. Doping further amplifies piezoresponse through morphological control. Undoped ZnO nanoparticles form 1D pencil-like nanorods or 2D nanosheets. Sinha *et al.* demonstrated that Y^{3+} doping induces a phase transition from 1D nanorods to 2D nanosheets [98]. The resulting Y-ZnO nanosheets exhibit an exceptional d_{33} of 420 pm/V, attributed to enhanced Y-O bond polarity *versus* Zn-O bonds. This promotes easier c-axis rotation under electric fields, substantially amplifying piezoelectric response.

Despite the dual functionality of ZnO as a piezoelectric and photocatalytic semiconductor, its piezocatalytic H_2O_2 production faces challenges from rapid recombination of piezopolarization charges. Rational catalytic site design for segregated e^- and h^+ transfer is essential to suppress disordered charge migration and active-site competition. Constructing metal-semiconductor Schottky heterojunction can deplete excess electrons in piezoelectrics, mitigating internal piezopotential screening [99]. For instance, Wen *et al.* engineered an Au–ZnO Schottky heterojunction for piezophotocatalytic H_2O_2 synthesis, facilitating dual ORR/WOR pathways [100]. This configuration achieved 186 μmol/L H_2O_2 in pure water within 30 min, where reduction reactions exclusively localized to Au sites while oxidation reactions occurred at ZnO domains. This spatial isolation of active sites suppresses competitive adsorption, thereby facilitating synergistic coupling of oxidation–reduction processes.

Morphological engineering, metal/nonmetal doping, defect engineering, and heterostructure construction constitute effective strategies for optimizing the piezocatalytic performance of ZnO. Morphological control enhances built-in electric fields and elevates piezoelectric coefficients through tailored nanostructures. Doping strategies enhance polarization levels and boost active site density, while defect engineering strengthens reactant adsorption and activation through strategically introduced vacancies. Heterojunctions facilitate charge separation by establishing interfacial built-in electric fields. Future efforts should integrate multidimensional synergy among these strategies while leveraging piezo-photocatalytic coupling to advance H_2O_2 production efficiency.

Optimizing ZnO piezocatalytic performance necessitates synergistic integration of morphological engineering, metal/nonmetal doping, defect engineering, and heterostructure construction. Morphological control elevates piezoelectric coefficients by intensifying built-in electric fields through nanostructural tailoring, while doping strategies enhance polarization levels and active site density. Moreover, defect engineering strengthens reactant adsorption and activation *via* controlled vacancy generation. Concurrently, het-

erojunctions facilitate charge separation through interfacial built-in fields. Leveraging multidimensional synergistic interactions among these approaches, complemented by external assistance mechanisms such as piezoelectric photocatalysis, is poised to substantially advance H_2O_2 production.

2.2.4. Transition metal dichalcogenides

Transition metal dichalcogenides (TMDCs) consist of transition metal atoms (*e.g.*, Mo, W, Nb, Ta) bonded to chalcogen atoms (S, Se, Te) in stacked layered configurations (X – M – X), where M denotes the metal and X the chalcogen [101]. This stratified structure enables interlayer slippage or deformation under mechanical stress, thereby generating piezoelectric responses [102]. When transitioning from multilayer to monolayer, TMCDs undergo significant band structure transformations, such as indirect-to-direct bandgap transitions, thereby critically modulating piezoelectric properties.

Within TMDC materials systems, reducing dimensionality enhances piezoelectric performance. Monolayer TMDCs exhibit pronounced piezoelectric responses due to synergistic effects of reduced thickness and weakened interlayer coupling, which amplify lattice distortion [103]. Wang *et al.* experimentally demonstrated that thin MoS_2 flakes with odd-numbered atomic layers generate measurable piezoelectric voltage and current outputs during cyclic stretching/release, whereas even-layered and bulk MoS_2 exhibit negligible response [104]. MoS_2 nanosheets possess asymmetric odd-layer configurations, high electrical conductivity, abundant active edge sites, strong piezoelectric response, and large surface area (Fig. 4e) [105]. Monolayer MoS_2 adopts a S–Mo–S sandwich structure with a thickness of 0.62 nm, exhibiting a piezoelectric coefficient of 3.06 pm/V [106]. Intralayer Mo–S covalent bonds provide structural rigidity, while adjacent layers interact *via* weak van der Waals forces. In unstrained configurations, charge centroids coincide yielding zero net dipole moments. Under tensile strain, elongated Mo-S dipoles expand the unit cell, consequently inducing spontaneous polarization from S to Mo atoms. Conversely, compressive strain reverses polarization direction. The collective dipole realignment establishes an ordered unidirectional field parallel to the applied force. This polarization field drives efficient charge separation, migrating free carriers to material surfaces where they trigger redox reactions [107].

The piezocatalytic activity of TMDCs exhibits strong phase dependence across crystalline structures, 1T (trigonal), 2H (hexagonal), and 3R (rhombohedral). Notably, 2H-WS_2 demonstrates markedly higher activity than its 1T counterpart due to non-centrosymmetric symmetry, whereas the latter's centrosymmetry suppresses piezoelectricity [108]. However, while piezocatalysis relies on both layer thickness and phase structure, the high-activity 2H phase typically forms in multilayers/bulk configurations where diminished surface-area-to-volume ratios limit efficacy. Synthesizing few-layer 2H-dominant WS_2 and analogous TMDCs thus remains challenging. Meng *et al.* addressed this limitation through magnetic-induction-heated synthesis of Fe-doped WS_2 (Fe/WS_2) monolayers with enriched 2H phase [109]. Under 30 kHz ultrasound, Fe/WS_2 achieved 4680 μmol g^{-1} h^{-1} H_2O_2 production *via* selective ORR, a 47-fold enhancement over pristine WS_2.

The distinctive layered architecture of TMDCs delivers high specific surface areas and abundant active sites, as confirmed by recent research. Critically, piezoelectricity-induced built-in electric fields enable efficient charge carrier separation, positioning TMDCs as highly promising materials for piezocatalytic applications including H_2O_2 synthesis and pollutant degradation. To maximize catalytic performance, precise regulation of layer count and crystalline phase becomes essential, maximizing edge-site exposure while synergistically coupling the metallic conductivity of 1T phases with the intrinsic activity of 2H phases. This fundamental optimization must be coupled with *in-situ* characterization to establish explicit structure-function relationships, correlating layer thickness, phase composition, and piezoelectric response to propel rational design of advanced piezocatalysts.

2.2.5. Carbon-based materials

Graphitic carbon nitride (g-C_3N_4), a layered carbon-based catalyst, has gained significant attention in electrochemical applications due to its excellent conductivity and stability [110–113]. Its structure comprises *s*-triazine units interconnected *via* amino groups or nitrogen bridges, forming stratified layers. Three *s*-triazine units covalently link to create heptazine rings (C_6N_7). Periodic arrangement of these rings in 2D planes generates geometrically constrained triangular cavities [114]. Although bulk g-C_3N_4 is centrosymmetric, these cavities disrupt local symmetry, enabling strain-induced charge separation (flexoelectric effect). Meanwhile, stress-induced dipole realignment at cavity-edge polar bonds confers piezoelectricity. Both effects are synergistically amplified by uniform cavity distribution [115]. While pristine g-C_3N_4 exhibits an in-plane piezoelectric coefficient of only 10 pm/V, strategies such as morphological engineering, vacancy construction, and elemental doping will significantly enhance its piezoresponse [116].

Morphological engineering optimizes energy absorption pathways, enabling piezocatalysts to achieve greater deformation under identical mechanical energy input. Enhanced strain sensitivity promotes piezoelectric charge generation and catalytic efficiency [69]. For instance, Wang *et al.* synthesized diverse g-C_3N_4 structures, hollow nanotubes ($d_{33} = 34.99$ pm/V), nanosheets ($d_{33} = 14.44$ pm/V), and nanospheres ($d_{33} = 12.21$ pm/V) [117]. Under ultrasound, hollow nanotubes achieved 262 μmol g^{-1} h^{-1} H_2O_2 production, surpassing nanosheets and nanospheres by 1.5-fold and 6.2-fold, respectively. Concurrently, vacancy engineering enhances structural asymmetry and charge separation. Fu *et al.* engineered oxygen-doped, nitrogen-deficient C_3N_{5-x}-O piezocatalysts (Fig. 5a) [118], where dual defects (O-doping + *N*-vacancies) amplify asymmetry, expose triangular cavities, optimize band structures, and redistribute charges in ultrathin layers. This synergistic modulation enhanced piezoelectricity and active surface area, achieving 615 μmol g^{-1} h^{-1} H_2O_2 yield in pure water, a 6-fold increase over pristine g-C_3N_4.

Moreover, strategic incorporation of functional groups effectively enhances piezoelectric response and consequently optimizes electron transfer efficiency. Fu *et al.* engineered cyano groups (–C≡N) and nitrogen vacancies into C_3N_5, creating C_3N_{5-x}-CN with synergistic piezoelectric-photoelectric enhancement [119]. Critically, dual-defect sites amplified piezoelectricity and promoted charge carrier separation, boosting the piezo-photocatalytic H_2O_2 yield to 1359 μmol g^{-1} h^{-1} in pure water. Beyond vacancy engineering, perylene diimide (PDI), characterized by a rigid π-conjugated plane, represents a highly promising modifier for g-C_3N_4 [120]. Through its aromatic plane, PDI enhances π-π stacking with triazine rings while concurrently inducing planar distortion in layered g-C_3N_4, substantially amplifying polarization and boosting piezoelectric response [121]. Tang *et al.* demonstrated that PDI incorporation reinforces π–π interactions (facilitating electron migration) while distorting g-C_3N_4 layers into polar porous structures, achieving 149.8 μmol g^{-1} h^{-1} piezocatalytic H_2O_2 (twice the photocatalytic yield). Piezo-photocatalytic synergy further elevated production to 625.54 μmol g^{-1} h^{-1} [122].

Carbon-based piezoelectric catalysts demonstrate superior stability and durability in complex pH environments compared to metal-based counterparts, effectively mitigating environmental risks associated with heavy metal ion leaching. Their intrinsic metal-free nature offers compelling advantages in eco-compatibility and sustainability while simultaneously reducing material costs and long-term ecotoxicity risks. Nevertheless, the piezocatalytic performance of carbon-based materials remains un-

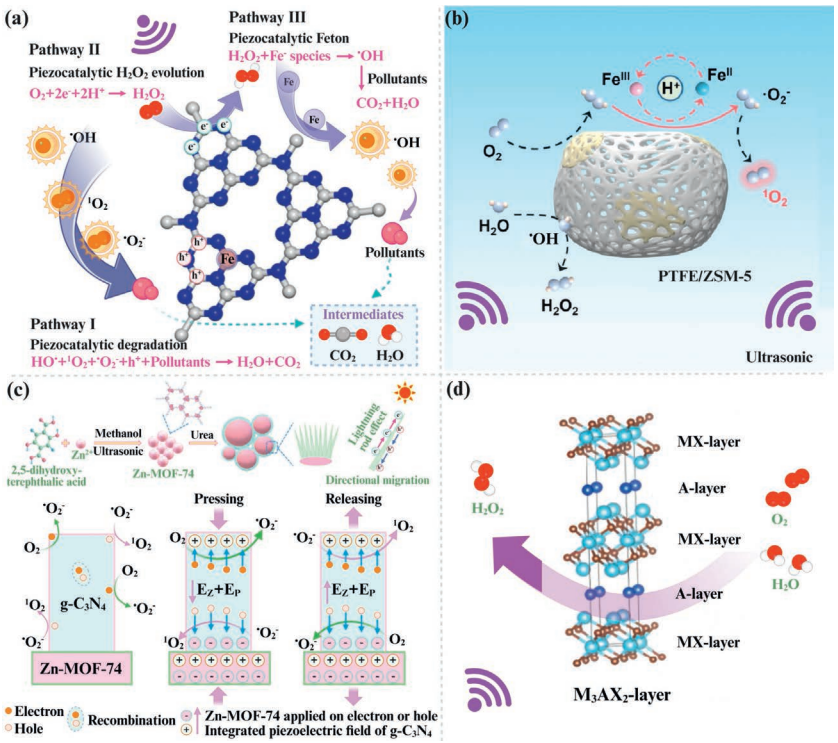


Fig. 5. Piezocatalytic H_2O_2 production in (a) carbon-based materials, (b) polymers, (c) MOFs, and (d) MAX phase materials systems. (a) Reproduced with permission [118]. Copyright 2023, Elsevier. (b) Reproduced with permission [127]. Copyright 2024, Wiley. (c) Reproduced with permission [133]. Copyright 2024, Elsevier. (d) Reproduced with permission [136]. Copyright 2023, Elsevier.

derexploited due to inherent limitations: The scarcity of non-centrosymmetric crystal structures and suboptimal piezoelectric polarization responses. Targeted catalyst design requires synergistic integration of structural engineering through defect manipulation (vacancies/edge sites) and heteroatom doping (N/B/P) to modulate electron distribution, simultaneously incorporating porous/hierarchical architectures for enhanced strain sensitivity. This foundational approach must be coupled with polarization optimization *via* electric poling or interfacial engineering using polar materials to directionally align dipoles, thereby enabling multi-field synergy where optical, thermal, and ultrasonic energies collectively amplify piezoresponse. Ultimately, computational modeling and *in-situ* characterization are essential to establish explicit structure-function relationships for precision-engineered catalyst development.

2.2.6. Polymers

The piezoelectricity of polymeric materials primarily originates from either spontaneously polarized ferroelectric phases or crystalline phases with asymmetric centers [123]. Enhanced piezoelectric performance is achieved by reorienting randomly aligned dipoles within polymer crystals through processing techniques, notably mechanical stretching or thermal/electrical poling under DC fields, thereby optimizing dipole alignment [71]. Ultimately, variations in piezoelectric response across polymeric systems are governed by disparities in molecular asymmetry and orientation fidelity [124].

PVDF exhibits five crystalline phases (α, β, γ, δ, ε), with the β-phase demonstrating superior polarity. Controlling β-phase content and crystalline orientation is therefore critical for fabricating high-performance PVDF piezoelectric/ferroelectric materials [125]. Meng *et al.* enhanced β-phase content and electrical conductivity by incorporating conductive polyaniline (PANI) into PVDF, synthesizing novel PANI/β-PVDF microspheres. The pristine PVDF powder exhibited the lowest piezoelectric coefficient ($d_{33} = 0.29 \times 10^{-11}$ C/N), while β-PVDF showed an 89.3 % increase in d_{33}. After PANI incorporation, d_{33} further rose to 3.50×10^{-11} C/N. These PANI/β-PVDF microspheres achieved exceptional piezocatalytic efficiency, degrading 98.1 % levofloxacin within 30 min.

PTFE exhibits significant potential as a piezocatalytic material for H_2O_2 generation. Wang *et al.* ultrasonicated PTFE stirring bars in aqueous media for 2 h, achieving H_2O_2 concentrations of 514.2 μmol/L [126]. The mechanism initiates with electrons transfer from oxygen atoms of water molecules to the LUMO sites of PTFE, generating negatively charged PTFE species (PTFE(e^-)) and positively charged water radical cations ($H_2O^{\bullet+}$). PTFE(e^-) reduces O_2 to form $^{\bullet}O_2^-$ (the precursor for H_2O_2), while $H_2O^{\bullet+}$ undergoes proton transfer with neutral H_2O to yield ·OH and hydronium ions (H_3O^+). Ultimately, ·OH radicals recombine to produce additional H_2O_2. Critically, intense interfacial electric fields generated by polarized C-F bonds during piezocatalysis reduce reaction activation energies. Compared to dielectrics like polyethylene (PE) and polyvinyl chloride (PVC), fluorinated polymers (FEP/PTFE) exhibit higher charge densities in contact-separation processes, producing stronger interfacial fields. However, inherent hydrophobicity limits aqueous dispersion and active site accessibility. To overcome this, Li *et al.* synthesized hydrophilic PTFE/ZSM-5 composites with uniform PTFE dispersion (Fig. 5b) [127], achieving an exceptional H_2O_2 production rate of 1978.8 μmol g^{-1} h^{-1}.

The piezoelectricity of polymeric materials originates from intrinsically polarized ferroelectric phases or asymmetric crystalline structures (*e.g.*, β-phase PVDF). Performance optimization requires dipole alignment through mechanical stretching or electric poling. Specifically, for PVDF, its β-phase, exhibiting the strongest polarity, serves as the cornerstone for high-performance applications. Compositing with conductive polymers (*e.g.*, polyaniline) synergistically enhances β-phase content and electrical conductivity. Thus, novel polarization techniques (electric field/strain co-modulation) and

additives (nanofillers/ionic liquids) can directionally induce β-phase formation and optimize molecular alignment, significantly amplifying piezoresponse. Meanwhile, PTFE demonstrates high piezocatalytic potential for H_2O_2 generation *via* strong interfacial electric fields from polarized C-F bonds. However, inherent hydrophobicity restricts dispersion and active-site accessibility. Addressing this necessitates functionalized carriers (porous oxides/carbon matrices) or surface modifications to balance hydrophilicity and interfacial charge enrichment. Furthermore, flexible heterojunctions (*e.g.*, PVDF/PTFE membranes) leverage synergistic polarization to augment catalytic efficiency. Collectively, multiscale structural engineering enables piezoelectric polymers to transcend inorganic material limitations, positioning them as core candidates for green catalysis and intelligent responsive technologies.

2.2.7. Metal organic frameworks

Metal organic frameworks (MOFs) are crystalline materials comprising metal ions/clusters interconnected by organic linkers, featuring high porosity and large specific surface areas [128–130]. Compared to conventional piezocatalysts, MOFs exhibit enhanced piezocatalytic activity and charge separation efficiency due to their polar functional groups and asymmetric structural units [131]. Huang *et al.* synthesized an aluminum-based MOF (NH_2−MIL-101(Al)) demonstrating a significant piezoelectric response (18.2 nm/V) under mechanical stress [132]. Ultrasonication induces structural distortion in NH_2−MIL-101(Al), generating bound charge polarization *via* displacement of positive/negative charge centers. This creates a polarized electric field that drives directional charge carrier migration, achieving an exceptional H_2O_2 production rate of 8890 μmol g^{-1} h^{-1}. Moreover, Li *et al.* developed a sea-urchin-like Zn-MOF-74@g-C_3N_4 composite through epitaxial growth of g-C_3N_4 nanoneedles on spherical Zn-MOF-74 substrates (Fig. 5c) [133]. This unique architecture leverages high-curvature needle tips to generate a lightning-rod effect that directs electron migration along the axial direction, thereby accelerating surface charge separation, while the established S-scheme heterojunction concurrently enhances bulk charge separation. Critically, coupling piezoelectric polarization with interfacial electric fields suppresses both surface and bulk charge recombination, significantly boosting charge transfer efficiency. Under combined piezocatalysis and photocatalysis, the composite achieved an H_2O_2 production rate of 697 μmol g^{-1} h^{-1}, surpassing pristine g-C_3N_4 and Zn-MOF-74 by 5.0- and 5.4-fold respectively. This performance stems from polarization-field synergy, which enhances charge carrier mobility and maximizes photogenerated electron/hole flux to catalytic surfaces and reactive interfaces, thus accelerating reaction kinetics and elevating H_2O_2 yield.

While conventional piezoelectric materials predominantly consist of inorganic ceramics or polymers, the piezoelectric properties of MOFs have garnered significant attention only in recent years. Their piezoelectric performance relies on non-centrosymmetric structures formed between metal clusters and organic linkers, but most MOFs exhibit high crystallographic symmetry that impedes spontaneous polarization. Through rational engineering of structural polarization, developing novel MOF-based materials as state-of-the-art piezocatalysts holds substantial practical potential for H_2O_2 generation across complex environmental conditions. Therefore, strategic enhancement of MOF piezocatalysts involves coupling MOFs with conductive substrates (*e.g.*, MXenes) or 2D nanosheets to augment charge transport efficiency and electrical conductivity, while simultaneously incorporating metal nanoparticles (Au, Pt) or functionalized ligands to optimize O_2 adsorption kinetics and refine electron transfer dynamics.

2.2.8. MAX phase materials

MAX phase materials, as emerging layered ternary compounds, have demonstrated unique potential in piezoelectric properties and catalytic applications. Their crystal structure features alternating stacks of $M_{n+1}X_n$ layers and A-element layers, with this non-centrosymmetric layered configuration enabling intrinsic piezoelectric responses [134]. Piezoelectric effects typically rely on crystallographic non-centrosymmetry, and the low-symmetry layered arrangement of MAX phases facilitates separation of positive/negative charge centers under mechanical stress, generating polarized electric fields [135]. Jia *et al.* systematically investigated MAX phases (*e.g.*, Ti_3AlC_2, Ti_3AlCN, Ti_3SiC_2) for piezocatalytic H_2O_2 production (Fig. 5d) [136]. The results demonstrate that Ti_3SiC_2 achieved the maximal H_2O_2 production rate of 871.0 μmol g^{-1} h^{-1} in pure water, surpassing the performance of predominant piezocatalysts. Besides, Tan *et al.* reported experimental evidence of piezoelectricity in monolayer $Ti_3C_2T_x$ MXene [48]. Surface functional groups (T_x) break crystal symmetry, endowing piezoelectricity. Under 1.08 % tensile strain, $Ti_3C_2T_x$ generated an intrinsic piezoelectric current of 0.3 nA, with a power density of 6.5 mW/m^2 and conversion efficiency of 11.15 %, exceeding all reported 2D materials.

Despite limited experimental data on MAX phase piezoelectricity in current literature, their unique combination of metallic conductivity and ceramic-like mechanical properties (*e.g.*, high hardness, thermal stability) may enable exceptional charge carrier transport pathways and structural robustness for piezocatalysis. Surface modification of A-site atoms (*e.g.*, Al, Sn) could enhance adsorption of O_2 or H_2O. Integrating MAX phases as reinforcing phases with semiconductors (*e.g.*, g-C_3N_4) may modulate interfacial electric fields to optimize charge separation efficiency, offering novel strategies for composite design. Furthermore, one-dimensional MAX phase nanofibers, with high specific surface area and mechanical flexibility, could improve stress responsiveness and active site distribution in piezocatalytic reactions. Although research on MAX phases in piezocatalysis remains nascent, their structural tunability, electrical conductivity, and mechanical stability provide distinct advantages for efficient H_2O_2 production. Future advancements require synergistic efforts in material design (*e.g.*, dimensionality engineering, surface functionalization) and mechanistic studies (*e.g.*, polarization response optimization, catalytic pathway refinement) to unlock their potential in green energy initiatives and environmental remediation.

3. Applications of piezocatalytic in wastewater remediation

3.1. Oxidation of organic pollutants

Piezocatalytic H_2O_2 production overcomes limitations of traditional synthesis by offering a green, low-energy alternative for wastewater treatment. These systems leverage dual pollutant degradation mechanisms through direct oxidation coupled with synergistic activation [137]. Mechanical stress induces piezoelectric polarization to generate built-in electric fields that simultaneously drive H_2O_2 production and micropollutant degradation (Fig. 6a) [138,139]. For example, hydroxyapatite demonstrates representative $2e^-$-ORR behavior where ultrasonication dissociates adsorbed water/hydroxide ions to release electrons enabling sequential single-electron transfers for H_2O_2 generation, subsequently driving efficient micropollutant degradation [140]. Complementarily, Peng *et al.* developed $Bi_3O(PO_4)_2OH$ microcrystals where enhanced -OH group asymmetry amplifies piezoelectric responses in phosphate units [141]. This dual-pathway system ($2e^-$-ORR + $2e^-$-WOR) achieved 639.11 μmol g^{-1} h^{-1} H_2O_2 yield under mild ultrasound (80 W, 40 kHz), with degrading 0.6 mg/L atrazine within 20 min.

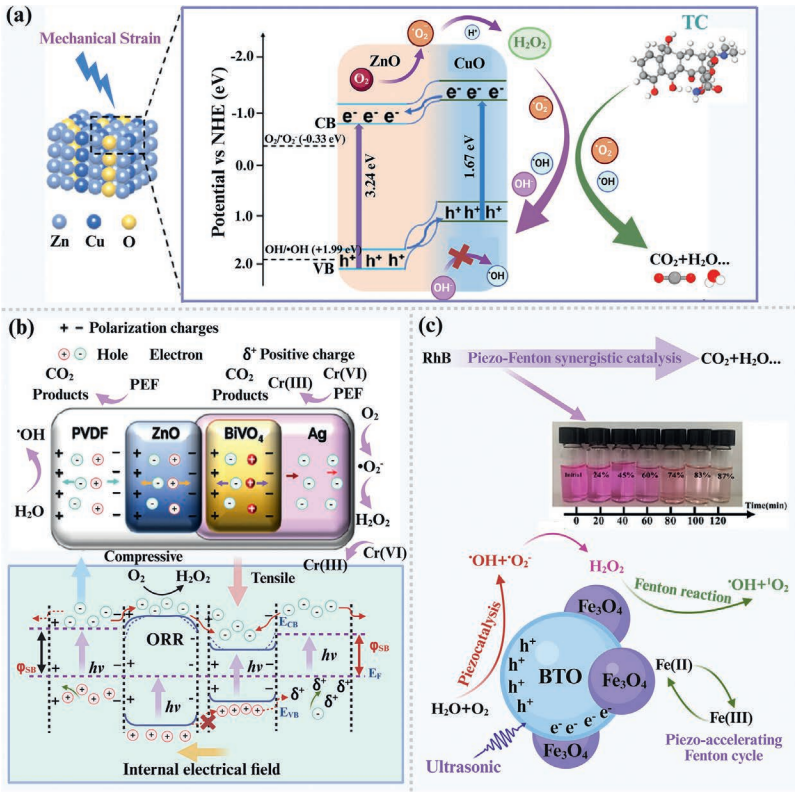


Fig. 6. Application of piezoelectrically generated H_2O_2 in organic compound oxidation. (a) Degradation of organic pollutants by ZnO/CuO piezoelectric nanocatalysts. Reproduced with permission [138]. Copyright 2023, ACS. (b) Simultaneous piezophotocatalytic H_2O_2 generation and removal of pefloxacin/Cr(VI) using $BiVO_4$/Ag-modified ZnO@PVDF coaxial nanofibers. Reproduced with permission [145]. Copyright 2024, Elsevier. (c) Piezo-Fenton catalytic degradation of RhB by Fe_3O_4-$BaTiO_3$ nanocomposites. Reproduced with permission [152]. Copyright 2024, Elsevier.

Beyond direct organic oxidation by H_2O_2, hole-mediated oxidation constitutes a complementary degradation pathway. Wang *et al.* revealed that during hole-electron separation, h^+ generated at $Fe_2(MoO_4)_3$ heterojunctions could oxidatively degrade electron-rich pollutants (*e.g.*, bisphenol A, phenytoin, ciprofloxacin), underscoring the necessity of enhancing h^+ concentration for efficient oxidant development targeting micropollutant degradation [142]. Similarly, electrochemically hydrogenated MoO_3 nanoparticles exhibit a narrowed bandgap that facilitates h^+ generation, resulting in H-MoO_3 with enhanced degradation efficiency for antibiotics [143]. Moreover, coupling piezoelectric catalysis with photocatalysis simultaneously enhances charge carrier separation through mechanical stress and photoexcitation, thereby boosting both H_2O_2 production and pollutant oxidation efficiency. The piezoelectric effect harnesses mechanical vibration energy to generate a polarized electric field that accelerates the separation and migration of photogenerated electron-hole pairs while suppressing recombination [144]. Demonstrating this synergy, Lv *et al.* employed $BiVO_4$ and Ag-decorated ZnO@PVDF nanofibers for piezo-photocatalytic ROS generation (H_2O_2, $^{\bullet}O_2^-$, $^{\bullet}OH$), achieving 147.7 μmol H_2O_2 production in 90 min with concurrent 95 % pefloxacin degradation within 30 min (Fig. 6b) [145]. Besides, Fu *et al.* introduced cyano groups (-CN) and N vacancies into semiconductor C_3N_5, successfully synthesizing an efficient piezo-photocatalyst (C_3N_{5-x}-CN) with enhanced piezo-photocatalytic performance [119]. The prepared C_3N_{5-x}-CN exhibited synergistic enhancement of piezoelectricity and photoelectricity in an ultrasound-assisted photocatalytic system, producing H_2O_2 at a rate of 1359 μmol g^{-1} h^{-1} and efficiently removing tetracycline with a rate constant of 0.0342 min^{-1}, which increased to 0.0492 min^{-1} in the presence of peroxymonosulfate (PMS). The piezopolarization process generates a large number of h^+, which act as strong oxidants capable of directly oxidizing pollutant molecules through contact. The efficiency of this process is influenced by the interaction between the pollutant and the catalyst surface. This hole-mediated oxidation offers the potential for selectively degrading specific types of pollutants, particularly effective for those that are recalcitrant under certain conditions.

Furthermore, $^{\bullet}OH$ serve as highly effective reactive species for micropollutant degradation due to their potent oxidative capacity ($E^0 = 2.80$ V/NHE). Therefore, introducing activators (such as Fe^{2+} or heterogeneous catalysts) enables the efficient conversion of H_2O_2 into highly oxidizing $^{\bullet}OH$, significantly enhancing oxidation capacity [146–148]. The Fenton technology based on H_2O_2 and Fe^{2+} is currently one of the most effective wastewater treatment methods, but it is severely constrained by challenges in Fe^{2+} regeneration and the continuous consumption of H_2O_2. Considering that the piezocatalytic process can generate electrons for Fe^{3+} reduction and generate H_2O_2 *in-situ*, it offers the potential to enhance Fenton reaction efficiency. The piezocatalytically generated H_2O_2 combines with introduced Fe^{2+} to produce $^{\bullet}OH$, forming a Fenton system capable of efficiently degrading organic pollutants [149]. For instance, ultrathin $Bi_{12}O_{17}Cl_2$ leverages $[Bi–O]_n$ interlayer-enhanced polarization to drive 2e$^-$-ORR pathways, achieving 7.76 mmol g^{-1} h^{-1} H_2O_2 production. With Fe^{2+} addition, its apparent rate constant for acetaminophen degradation reached 0.023 min^{-1} [70]. Similarly, ferroelectric $BaTiO_3$ nanoparticles under ultrasonic vibration enhance charge separation, promoting the formation of H_2O_2, and demonstrate effective degradation of various organic dyes [150]. The addition of Fe^{2+} further accelerates $^{\bullet}OH$ generation *via* Fenton-mediated H_2O_2 activation, achieving Congo red degrada-

tion at $k = 0.337\ min^{-1}$, a 6.4-fold enhancement over piezocatalysis alone.

Conventional Fenton systems predominantly utilize Fe^{2+} as an activator to decompose H_2O_2 (generated *via* $2e^-$-ORR) for pollutant degradation. However, kinetic competition between ORR and Fe^{3+} reduction, coupled with the difficulty in initiating water oxidation reactions, severely limits overall Fenton efficiency [84]. An ideal strategy integrates $2e^-$-WOR for H_2O_2 generation with Fe^{3+} to Fe^{2+} reduction, simultaneously leveraging electrons and holes to maximize efficiency. To overcome the high thermodynamic barrier (>1.76 V) of $2e^-$-WOR, piezocatalysis provides separated charges that facilitate Fe^{3+} reduction, enabling piezo-self-Fenton (PSF) systems. Xu *et al.* developed a $BiOIO_3$ piezocatalyst for $2e^-$-WOR for H_2O_2 generation [151]. When coupled with Fe^{3+}, it simultaneously drives WOR-H_2O_2 generation and Fe^{3+} reduction, enabling rapid subsequent Fenton reactions. The Fe^{3+}-mediated PSF system exhibited a sulfamethoxazole degradation rate constant 3.5-fold higher than conventional Fe^{2+}-PSF systems. Complementarily, Li *et al.* enhanced PTFE dispersion on ZSM-5, attaining 1978.8 μmol g^{-1} h^{-1} H_2O_2. Fe^{3+}-initiated Fenton reactions activated H_2O_2 decomposition, degrading >99 % azo dyes in 10 min, which 6-fold faster than standalone piezocatalysis [127]. Despite progress, current piezo-Fenton systems often employ non-recoverable nanoparticles and soluble Fe^{2+}, risking secondary contamination. Xie *et al.* addressed this by synthesizing Fe_3O_4-$BaTiO_3$ nanocomposites, enabling self-contained piezo-Fenton processes without external additives (Fig. 6c) [152]. This system achieved 98.2 % dye degradation in acidic solutions, surpassing pure piezocatalysis and conventional Fenton by 33 % and 67 %, respectively. In summary, synergistic activation strategies, converting H_2O_2 to highly oxidative radicals, outperform direct oxidation in complex matrices by minimizing chemical consumption and extending operational longevity, particularly for recalcitrant pollutants. Consequently, future catalyst designs must prioritize recoverability for practical implementation. Integrating piezoelectric materials with magnetic ferrites addresses the unrecoverability limitation of conventional piezocatalysts, preventing secondary contamination while establishing a sustainable paradigm for piezo-Fenton systems.

3.2. Polymerization of organic pollutants

From a carbon-cycle perspective in water purification, oxidative polymerization offers distinct advantages over organic pollutant mineralization. It directly converts aqueous organic contaminants into solid organic polymers, enabling organic carbon recovery while mitigating the carbon-intensive drawbacks (high energy consumption and emissions) of conventional mineralization processes [153]. In H_2O_2-based advanced oxidation processes, ·OH abstracts hydrogen atoms from functional groups (R-H) of organic substrates to generate organic radicals (R·) [154]. While sufficient ·OH flux drives these radicals toward oxidative degradation and ultimate mineralization, substoichiometric ROS levels shift the pathway toward radical polymerization. Under such limited ROS conditions, characteristic of piezocatalytic systems, R· or hydroxylated radical intermediates (R·-OH) undergo polymerization reactions. This creates an inherent advantage for piezocatalytic systems where limited ROS generation favors polymerization pathways (Fig. 7a) [155]. Aromatic radical cations form radical monomers *via* electron transfer and hydrogen atom elimination. During polymerization, alkoxy radicals (R·) and aromatic radicals (*e.g.*, phenoxyl radicals PhO·) serve as key intermediates for coupling and chain propagation [156]. Chain reactions proceed through monomer radical oxidation to dimers, forming dimer radicals (R_2·), while chain growth involving monomers and phenolic radicals generates R_{n-1}·. Chain termination occurs when propagating radicals combine with R·, yielding R_n [157]. Significantly, piezocatalytic systems

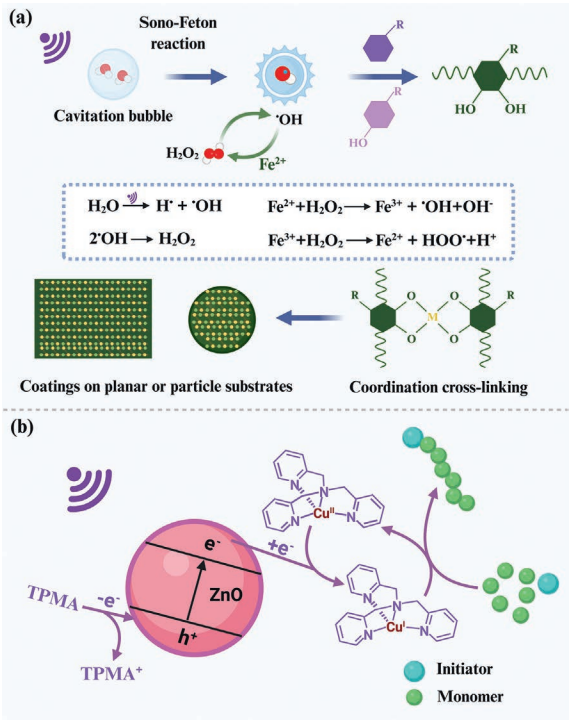


Fig. 7. Application of piezoelectricity in organic polymerization. (a) Phenolation and film formation mediated by iron-ion-promoted ·OH generation during piezoelectric catalysis. Reproduced with permission [155]. Copyright 2021, Wiley. (b) Enhancement of mechanically induced atom transfer radical polymerization (ATRP) *via* piezoelectrically promoted interfacial electron transfer from nanoparticles to Cu catalysts. Reproduced with permission [162]. Copyright 2017, ACS.

inherently yield controlled concentrations of ·OH, which function as initiators for polymer synthesis. This intrinsic polymerization propensity originates from synergistic interplay between bulk oxidative capacity and specific surface structures. Consequently, strategic modulation of catalyst surface structures, *via* functional group engineering and geometric configurations, enables precise regulation of pollutant transformation pathways toward polymerization or mineralization by altering adsorption energies and electrostatic potentials of pollutants and their intermediates.

The initiation of polymerization pathways relies on limited radicals that trigger coupling reactions between pollutant molecules, forming macromolecular polymers immobilized on catalyst surfaces [158]. Critically, interactions between organic compounds and catalysts play a decisive role in determining oxidation pathways and mechanisms. Chen *et al.* revealed that in Fhy/H_2O_2 systems, compounds containing -COOH groups exhibit highly selective oxidation due to complexation with surface Fe(III) sites [154]. Conversely, compounds incapable of such interactions follows distinct oxidation mechanisms. Liu *et al.* engineered single-atom Cu on MgO to drive PMS-based Fenton reactions [159]. They demonstrated that shifting the Cu configuration from lattice-embedded to surface-loaded fundamentally altered the catalytic pathway. The optimized catalyst achieved near-complete removal of phenolic compounds *via* polymerization, significantly enhancing oxidant utilization efficiency. These findings underscore the critical influence of catalyst interfacial design on polymerization selectivity.

Complementarily, direct electron transfer processes selectively extract electrons from organic compounds, particularly those containing aromatic or thiophene rings, followed by proton elimination to generate monomer radicals as key intermediates [160]. These radicals subsequently undergo coupling reactions, forming chain-like polymers [161]. Illustrating this principle,

Wang *et al*. developed a robust mechano-controlled atom transfer radical polymerization system. Under ultrasonication, mechanical energy induces electron transfer from nanoparticle surfaces to deactivators (Cu^{II}/L), promoting the formation of activators (Cu^{I}/L) and thereby accelerating polymerization kinetics (Fig. 7b) [162]. Meanwhile, Ding *et al*. employed piezoelectric ZnO nanoparticles as mechanochemical transducers to achieve precisely controlled piezoelectric-mediated reversible addition–fragmentation chain transfer (RAFT) polymerization [163]. The resulting polymers exhibited high end-group fidelity, low dispersity, and efficient chain extension capabilities.

In recent years, piezocatalytically induced organic polymerization has demonstrated unique potential for the directional transformation of environmental pollutants. Within this process, the generated •OH radicals serve dual functions: They act as oxidants initiating pollutant degradation, and they also form radical monomers (*e.g.*, PhO•) through hydrogen atom abstraction (HAA) or single-electron transfer (SET). These monomers subsequently trigger coupling polymerization, yielding macromolecular polymers immobilized on catalyst surfaces, a process synergistically governed by the electronic states and spatial constraints of the catalyst surfaces. Notably, the polymerization pathway depends on the catalyst material. Metal-based catalysts (*e.g.*, Fe(III)/ferrihydrite, Ca-Mn-O perovskites) induce surface-dependent chain polymerization *via* direct oxygen transfer pathways (DOTP) or electron transfer processes (ETP), while carbon-based materials (*e.g.*, GP-COOFe(III)) preferentially catalyze oligomer formation. However, critical knowledge gaps persist regarding dynamic competition mechanisms among active species (•OH/HO_2^-/high-valent metal-oxo), quantitative relationships between radical initiation and chain termination, and impacts of polymer formation on piezoelectric deformation and charge separation. A particularly notable absence of studies concerns polymer-induced material strain and dipole moment alterations, creating a significant theoretical barrier to advancing piezocatalytic polymerization for deep wastewater remediation.

Future developments will prioritize multiscale catalyst interface engineering, advanced *in-situ* characterization techniques, and optimization of piezo-electrochemical coupling processes. These efforts aim to achieve efficient transformation of pollutants into benign polymers while concurrently enhancing oxidant utilization and energy efficiency. Significantly, advancements in mechano-driven piezocatalytic polymerization, epitomized by ultrasound-mediated atom transfer radical polymerization, are establishing a new paradigm that bridges synergistic innovation between wastewater remediation and functional material synthesis.

3.3. Piezoelectric disinfection

Piezocatalysis harnesses mechanical energy (*e.g.*, water flow, vibration) to drive piezoelectric materials, generating a polarized electric field. This field directly catalyzes the oxidation of water molecules or the reduction of oxygen molecules to produce H_2O_2. Crucially, this *in-situ*-generated H_2O_2 can be immediately utilized for on-site disinfection, effectively circumventing the high energy consumption and transportation leakage risks associated with traditional centralized H_2O_2 production [164]. Within piezocatalytic systems, ROS such as •OH and $•O_2^-$ exert antibacterial effects by disrupting bacterial cell membranes or penetrating cells to induce oxidative stress, ultimately leading to cellular dysfunction and death [165]. Demonstrating performance enhancement, Meng *et al*. significantly boosted the piezoelectric response of PVDF by incorporating Cu nanosheets (CuNS) [166]. The resulting CuNS 4 %/PVDF composite exhibited a piezoelectric coefficient 2.6-fold higher than pure PVDF. Under aeration, this system achieved a H_2O_2 production rate of 163.3 μmol g^{-1} h^{-1} *via* piezocatalysis. This *in-situ* generated H_2O_2 demonstrated exceptional disinfection efficacy, achieving 99.7 % bactericidal efficiency against *Escherichia coli*after 80 min of air aeration. Similarly, Yang *et al*. enhanced the piezoelectric properties of $BaTiO_3$ through sulfur doping, which improved electron-hole pair separation (Fig. 8a) [167]. The S-doped $BaTiO_3$ demonstrated exceptional piezocatalytic antibacterial performance, achieving 97.12 % antimicrobial efficiency against *S. aureus.* Further illustrating this potential, Banerjee *et al*. synthesized a ZnO/chitosan nanocomposite for disinfection (Fig. 8b) [168]. After 20 min of ultrasonication, this composite system achieved 96 % removal of *E. faecalis* and 98 % removal of *E. coli.* Collectively, these studies underscore the significant promise of piezocatalytically generated *in-situ* H_2O_2 for advanced disinfection applications.

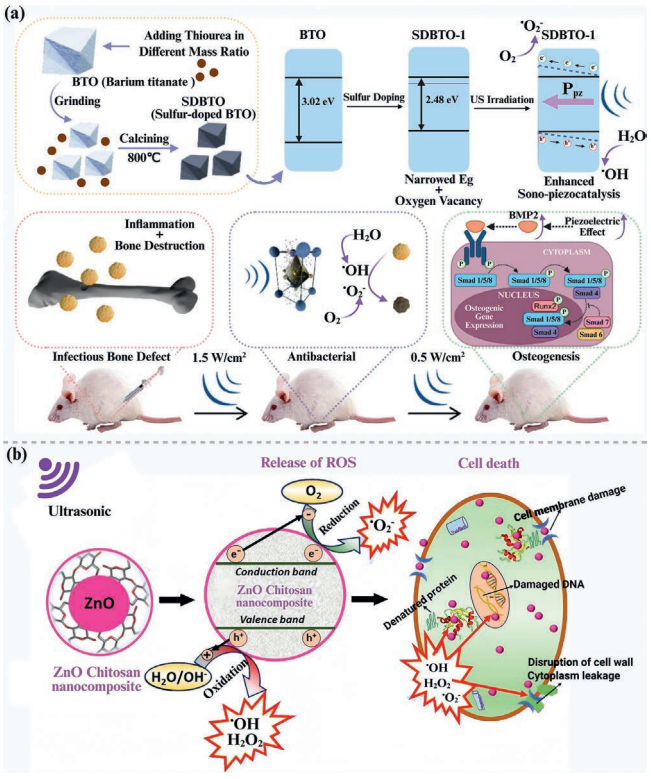


Fig. 8. Application of piezoelectricity effect in disinfection. (a) Piezocatalytic mechanism for antibacterial and osteogenic dual therapy. Reproduced with permission [167]. Copyright 2022, Elsevier. (b) H_2O_2 production process and its subsequent *in-situ* applications. Reproduced with permission [168]. Copyright 2024, Elsevier.

Beyond standalone disinfection, the ROS generation inherent in piezocatalytic H_2O_2 production systems enables the synergistic coupling of pollutant degradation and antibacterial action within a single process. Chen *et al*. exemplified this by developing a BiOCl piezocatalyst that achieved a high H_2O_2 production rate of 710 μmol g^{-1} h^{-1} through dual ORR/WOR pathways [169]. They engineered an integrated system for simultaneous H_2O_2 generation and efficient *in-situ* utilization, achieving 70.7 % antibacterial efficiency in wastewater alongside the synchronous degradation of sulfamethoxazole (SMX). Notably, when combining the piezocatalytic system with periodate activation, SMX removal reached 94.7 %, exhibiting reaction kinetics 10-fold faster than systems relying on externally added H_2O_2. This performance directly validates the practical feasibility of the "produce-and-use-immediately" approach in real-world scenarios, demonstrating that H_2O_2 production and functional utilization can be seamlessly coupled within a single system, eliminating the need for storage or transportation. This represents a critical advancement for the practical implementation of piezocatalytic technology. Furthermore, the combination of piezocatalytically generated H_2O_2 with other strong oxidants of-

fers a promising strategy to further enhance disinfection efficacy, providing valuable insights for future optimization of piezocatalytic antibacterial systems.

Piezocatalytic antibacterial technology holds significant promise for medical sterilization, food disinfection, and water treatment, primarily due to its inherent advantages of oxidant-free operation, residue-free output, and operational simplicity. Despite notable advancements, critical challenges persist in optimizing piezoelectric material performance and expanding practical applications. Paramount among these is the incomplete mechanistic understanding of antibacterial action, specifically how material properties govern ROS generation and cell membrane disruption pathways. Compounding this challenge, the relatively low piezoelectric coefficients of most currently reported materials significantly limit their effectiveness in antibacterial applications. Consequently, future research must prioritize the strategic design of material microstructures to enhance piezocatalytic antibacterial performance while ensuring long-term stability under sustained mechanical stress and diverse environmental conditions.

4. Conclusion and prospect

Piezocatalytic H_2O_2 production technology demonstrates promising application prospects due to its low material costs and clean, efficient reaction processes. However, the H_2O_2 yield remains limited primarily due to weak piezoelectric responses in catalysts, low mechanical-to-energy conversion efficiency, and insufficient active sites that hinder reactant adsorption and activation. More critically, fundamental challenges persist in elucidating H_2O_2 evolution mechanisms, conducting operando analysis of catalytic processes, achieving targeted structural modulation of piezoelectric catalysts, and developing effective H_2O_2 concentration-enhancement strategies, rendering current systems far from industrial implementation readiness.

Mechanistically, the $2e^-$-ORR is thermodynamically favorable yet kinetically limited, while the sequential single-electron pathway ($2 \times 1e^-$-ORR) exhibits superior kinetics but demands precise regulation of the $HO_2^{\bullet}$ adsorption-desorption equilibrium, requiring controlled adsorption energies (*e.g.*, −0.45 eV) to prevent over-reduction to H_2O, which imposes stringent requirements on catalyst active site design and electronic structure optimization. The $2e^-$-WOR suffers from low efficiency due to its high energy barrier ($E^0 \geq 1.77$ V/NHE) and competition with the $4e^-$-OER, though it holds unique advantages in oxygen-deficient systems like wastewater treatment. Coupling ORR and WOR pathways can enhance overall efficiency, yet their synergy remains unclear, and energy/mass transfer matching requires optimization. Advancing piezocatalysis toward industrial-scale green H_2O_2 synthesis thus necessitates constructing synergistic ORR/WOR systems by elucidating intermediate transfer mechanisms *via* operando techniques (*e.g.*, synchrotron radiation, *in-situ* FTIR) while expanding applications in oxygen-independent environments such as anoxic wastewater treatment.

At the material level, non-centrosymmetric structures facilitate driving forces through spontaneous polarization. However, critical challenges persist in addressing the temperature dependence (*e.g.*, Curie temperature limitations) and long-term stability of the piezoelectric coefficient d_{33}. Here, piezocatalytic H_2O_2 generation performance is intrinsically governed by multiscale structural characteristics: Crystal structures determine the intrinsic efficiency of piezoelectric polarization, where orientation of polar phases and defect density directly influence charge separation and surface redox activity; heterojunction interface engineering enhances carrier mobility while suppressing electron-hole recombination through band alignment; surface modifications using noble metals create reactive sites for intermediate adsorption and H_2O_2 pathway modulation; porous structures optimize mass transport channels and active site exposure *via* increased specific surface area; thickness and aggregation degree must balance mechanical robustness with charge transport efficiency, where excessive values constrain spatial responses to strain-induced polarization, while insufficient values compromise structural integrity. Through cross-scale optimization of crystal-interface-surface-pore-macro parameters, coupled with enhanced mechanical energy input modes and suppressed charge recombination, comprehensive improvements in piezoresponse, selectivity, and durability become achievable. Consequently, developing multifunctional materials (*e.g.*, 2D heterostructures, ferroelectric-semiconductor hybrids) that integrate high piezoresponse with stability, leveraging defect engineering and interfacial modulation to balance reaction pathway selectivity, while optimizing mechanical stress input *via* low-frequency, high-amplitude ultrasound or dynamic strain fields to maximize energy conversion efficiency and operational lifetime, establishes a robust material foundation for industrial-scale piezocatalytic applications.

Piezocatalysis leverages polarized built-in electric fields to generate *in-situ* H_2O_2, establishing it as a promising advanced wastewater remediation strategy. Structural asymmetry enhancement in piezoelectric materials achieves high H_2O_2 yields under mild ultrasonication, while coupling with photocatalysis concurrently elevates H_2O_2 production and enables complete organic mineralization through accelerated charge separation. To overcome the limited oxidative capacity of H_2O_2, self-sustaining PSF systems utilize piezoelectrons for continuous Fe^{3+}/Fe^{2+} cycling and H_2O_2 activation, thereby circumventing the bottleneck of conventional Fenton processes and broadening applications for deep pollutant removal. Simultaneously, the reactive species (h^+ and ROS) generated during piezoelectric processes effectively disinfect waterborne pathogens such as *E. coli*. On the other hand, in organic polymerization pathways, piezocatalytically derived $^{\bullet}OH$ initiates radical monomers *via* hydrogen abstraction and electron transfer, facilitating pollutant coupling into solid-phase polymers for resource recovery. Moreover, catalyst interfacial characteristics critically determine reaction pathway selection. Metal-based materials such as Fe(III)/ferrihydrite promote chain polymerization through DOTP, whereas carbon-based catalysts preferentially facilitate oligomer formation. Although ultrasound-driven mechanochemical polymerization achieves precise molecular weight control, the impact of piezoelectric deformation on polymerization kinetics remains to be elucidated.

Therefore, advancing piezocatalysis for deep wastewater purification requires prioritized development of piezo-photo-magneto multiphysics catalysts. Such systems optimize radical generation and electron transfer through interface engineering. Concurrently, establishing *in-situ* diagnostics will elucidate dynamic correlations among piezoelectric polarization, pollutant transformation, and material deformation, particularly polymer deposition impacts on piezoresponse. Additionally, designing pathway-specific conversion processes tailored to pollutant characteristics enables selective mineralization or controlled polymerization of recalcitrant contaminants *via* modulated redox potentials and surface adsorption energies. Furthermore, scaling up magnetic composite catalysts with enhanced cycling stability while developing cascade valorization pathways for polymeric products will prove pivotal for engineering implementation. Collectively, piezocatalysis drives a paradigm shift toward green, efficient, and resource-circular advanced water remediation.

CRediT authorship contribution statement

Yue Yin: Writing – original draft, Methodology, Investigation, Funding acquisition, Formal analysis, Data curation, Conceptualization. **Yaping Fan:** Visualization, Validation, Software, Project ad-

ministration. **Jiao Yang:** Writing – review & editing, Software, Methodology, Investigation, Formal analysis, Conceptualization. **Yi Ren:** Writing – review & editing, Software, Funding acquisition. **Bo Lai:** Writing – review & editing, Supervision, Methodology.

Declaration of competing interest

The authors declare that they have no known competing financial interest or personal relationships that could have appeared to influence the work reported in this paper.

Acknowledgments

This study was financially supported by National Natural Science Foundation of China (Nos. 22476187 and 22206173), Natural Science Foundation of Henan (No. 252300421179), Foundation of Henan Educational Committee (No. 25A610001), and Sichuan Science and Technology Program (No. 2025ZNSFSC0955). Graphical abstract and Figure 1–8 were created with BioRender.com.

Supplementary materials

Supplementary material associated with this article can be found, in the online version, at doi:10.1016/j.cclet.2026.112556.

References

[1] P. Haripriya, T. Anjana, K. Sreelakshmi, et al., Catal. Commun. 187 (2024) 106909.
[2] Z. Li, D. Shen, Q. Liu, et al., Chin. Chem. Lett. 36 (2025) 111045.
[3] W. Zhu, W. Zuo, P. Wang, et al., Chin. Chem. Lett. 35 (2024) 109341.
[4] X. Li, W. Fu, R. Guan, et al., Chin. Chem. Lett. 35 (2024) 109625.
[5] Z. Deng, S.J. Choi, G. Li, X. Wang, Chem. Soc. Rev. 53 (2024) 8137–8181.
[6] W.B. Cunningham, J.D. Tibbetts, M. Hutchby, et al., Green Chem. 22 (2020) 513–524.
[7] M.Z. Kassaee, H. Zandi, J. Akbari, E. Motamedi, Chin. Chem. Lett. 23 (2012) 470–473.
[8] H.Y. Guo, J.C. Li, Y.L. Shang, Chin. Chem. Lett. 20 (2009) 1408–1410.
[9] M. Melchionna, P. Fornasiero, M. Prato, Adv. Mater. 31 (2018) 1802920.
[10] Z. Chen, B. Yang, J. Li, et al., Chin. Chem. Lett. 36 (2025) 110320.
[11] Y. Hu, W. Yang, Y. Ma, et al., Nat. Commun. 16 (2025) 1692.
[12] Z. Du, Z. Zhou, N. Sun, C. Yue, F. Liu, Chin. Chem. Lett. 36 (2025) 111341.
[13] J. Li, N. Xu, Y. Zhang, et al., Chin. Chem. Lett. 35 (2024) 110470.
[14] M. Ran, B. Du, W. Liu, et al., Pro. Natl. Acad. Sci. U. S. A. 121 (2024) e2317435121.
[15] R. Hinchet, U. Khan, C. Falconi, S. Kim, Mater. Today 21 (2018) 611–630.
[16] F. Zheng, X. Wan, Y. Zhang, et al., Sci. Adv. 11 (2025) eads8694.
[17] Q. Zhang, Y. Jia, W. Wu, et al., Nano Energy 113 (2023) 108507.
[18] Y. Wang, X. Li, Y. Chen, et al., Adv. Mater. 35 (2023) 2305257.
[19] S. Mondal, K. Dilly Rajan, L. Patra, M. Rathinam, V. Ganesh, Small 21 (2025) 2411828.
[20] S. Lan, J. Feng, Y. Xiong, et al., Environ. Sci. Technol. 51 (2017) 6560–6569.
[21] H.C. Song, S.W. Kim, H.S. Kim, et al., Adv. Mater. 32 (2020) 2002208.
[22] L. Guan, D. Mehdi, H. Li, F. Chen, S. Jin, Chin. Chem. Lett. 36 (2025) 111389.
[23] C. Li, W. Liu, X. Chen, et al., Chin. Chem. Lett. 35 (2024) 109652.
[24] K.T. Wong, C.E. Choong, I.W. Nah, et al., Appl. Catal. B: Environ. 315 (2022) 121581.
[25] Y. Wang, X. Zhang, X. Guo, et al., J. Mater. Sci. 53 (2018) 13081–13089.
[26] H. Zeng, C. Yu, C. Liu, et al., Mater. Today Energy 39 (2024) 101475.
[27] P. Vaghefi, A. Baghizadeh, A. Lourenco, et al., Materials 10 (2017) 1107.
[28] Q. Nie, Y. Xie, J. Ma, J. Wang, G. Zhang, J. Clean. Prod. 242 (2020) 118532.
[29] J. Wu, N. Qin, D. Bao, Nano Energy 45 (2018) 44–51.
[30] H. Niu, H.Y. Kwon, T. Ma, et al., Nat. Commun. 15 (2024) 10199.
[31] Y. Chen, J. Liu, J. Yu, Y. Guo, Q. Sun, Phys. Chem. Chem. Phys. 21 (2019) 1207–1216.
[32] Y. Li, L. Li, F. Liu, et al., Nano Res. 15 (2022) 7986–7993.
[33] T. Zhang, Y. Li, L. Li, et al., Nano Energy 99 (2022) 107375.
[34] H. Ni, J. Guo, T. Yang, et al., Appl. Surf. Sci. 687 (2025) 162254.
[35] D. Tai, X. Zhao, T. Zheng, J. Wu, ACS Appl. Mater. Interfaces 15 (2023) 36564–36575.
[36] Q. Xiao, L. Chen, Y. Xu, W. Feng, X. Qiu, Appl. Surf. Sci. 619 (2023) 156794.
[37] P. Wang, X. Li, S. Fan, et al., Appl. Catal. B: Environ. 279 (2020) 119340.
[38] H. Cai, F. Chen, C. Hu, et al., Chin. J. Catal. 57 (2024) 123–132.
[39] L. Lai, H. Zhou, Y. Hong, et al., Chin. Chem. Lett. 35 (2024) 108580.
[40] X. Zhou, B. Shen, A. Lyubartsev, J. Zhai, N. Hedin, Nano Energy 96 (2022) 107141.
[41] Q. Xu, Y. Zhang, D. Lu, et al., ACS Appl. Nano Mater. 7 (2024) 17379–17390.
[42] Y. Ye, C. Zhao, J. Zhou, et al., Appl. Surf. Sci. 685 (2025) 162064.
[43] J. Xu, H. Che, C. Tang, B. Liu, Y. Ao, Adv. Mater. 36 (2024) 2404539.
[44] X. Zhou, B. Shen, J. Zhai, J. Yuan, N. Hedin, ACS Appl. Mater. Interfaces 16 (2024) 20472–20484.
[45] P.D.M. Phan, D.V. Nguyen, N.H. Anh, et al., ACS Appl. Nano Mater. 6 (2023) 16702–16715.
[46] W. Ma, S. Suo, S. Du, et al., Renew. Energy 247 (2025) 123027.
[47] M.T. Ahmed, H. Abdullah, D.H. Kuo, X.Y. Tian, J. Environ. Chem. Eng. 12 (2024) 113640.
[48] D. Tan, C. Jiang, N. Sun, et al., Nano Energy 90 (2021) 106528.
[49] J. Kim, M. Jang, G. Jeong, et al., Nano Energy 89 (2021) 106409.
[50] Z. Gao, M. Li, Y. Sun, W. Yang, J. Hazard. Mater. 360 (2018) 436–444.
[51] Y. Zhou, H. Dong, Z. Xu, et al., Appl. Catal. B: Environ. 343 (2024) 123504.
[52] Y. Zhang, Y. Lin, R. Li, et al., Chem. Eng. J. 465 (2023) 143043.
[53] Y. Jiang, J. Xie, Z. Lu, et al., J. Colloid Interf. Sci. 612 (2022) 111–120.
[54] J. Chen, R. Xuan, Y. Dou, et al., ACS Appl. Polym. Mater. 6 (2024) 13671–13680.
[55] S. Wang, W. Tian, J. Han, et al., ACS Appl. Mater. Interfaces 15 (2023) 55129–55138.
[56] L. Liu, M. Ruan, C. Wang, Z. Liu, Appl. Catal. B: Environ. 354 (2024) 124117.
[57] W. Wang, Q. He, Y. Yi, et al., J. Clean. Prod. 415 (2023) 137818.
[58] F. Sehar, S. Anjum, A. Mansoor, Z. Mustafa, Appl. Phys. A 127 (2021) 718.
[59] M. Chai, W. Tong, Z. Wang, et al., J. Hazard. Mater. 430 (2022) 128446.
[60] Y. Zhu, H. Chen, L. Wang, et al., Chin. Chem. Lett. 35 (2024) 108884.
[61] C. Lin, G. Fan, J. Luo, et al., Chem. Eng. J. 520 (2025) 166094.
[62] J. Bhadra, D. Ponnamma, A. Alkareem, et al., Int. J. Energy Res. 46 (2022) 8503–8515.
[63] M. Pelayo Garcia, K.B. Saddik, M.S. Baghini, et al., Adv. Electron. Mater. 10 (2024) 2400138.
[64] I.E. Khalil, P. Das, H. Küçükkeçeci, et al., Chem. Mater. 36 (2024) 8330–8337.
[65] S. Kang, S. Jeon, S. Kim, et al., ACS Appl. Mater. Interfaces 10 (2018) 27424–27431.
[66] W. Gao, B. Xie, C. Ma, et al., Chem. Eng. J. 506 (2025) 160084.
[67] M. Zhu, B. Liao, Y. Tang, et al., Appl. Surf. Sci. 628 (2023) 157366.
[68] X. Wang, X. Hu, Z. Qu, et al., ACS Appl. Mater. Interfaces 16 (2024) 26257–26271.
[69] Z. Wang, G. Ding, H. Huang, et al., eScience 5 (2024) 100370.
[70] Y. Wu, P. Wang, H. Che, et al., Angew. Chem. Int. Ed. 63 (2024) e202316410.
[71] Z. Ye, J. Yi, Y. Zhang, et al., Adv. Mater. Technol. 10 (2024) 2401447.
[72] R. Wang, G. Xu, Y. He, e-Polymers 17 (2017) 215–220.
[73] M. Zatloukal, R. František, P. Sáha, Eur. Polym. J. 38 (2002) 1925–1927.
[74] O.B. Kaliuzhnyi, V.Y. Platkov, J. Polym. Res. 29 (2022) 32.
[75] E.A. Katz, Helv. Chim. Acta 103 (2020) e2000061.
[76] S. Parwaiz, M.M. Khan, J. Environ. Chem. Eng. 12 (2024) 113175.
[77] M.J. Zhou, T. Yang, J.J. Wang, et al., Acta Mater. 187 (2020) 146–152.
[78] X. Xu, Z. Wu, L. Xiao, et al., J. Alloy. Com. 762 (2018) 915–921.
[79] B. Khanbabaee, E. Mehner, C. Richter, et al., Appl. Phys. Lett. 109 (2016) 222901.
[80] H. Gao, Y. Zhang, H. Xia, et al., Colloids Surf. A: Physicochem. Eng. Asp. 663 (2023) 131031.
[81] E. Lin, J. Wu, N. Qin, et al., Catal. Sci. Technol. 9 (2019) 6863–6874.
[82] X. Wang, X. Wei, Q. Su, et al., Nano Energy 133 (2025) 110459.
[83] C. Wang, F. Chen, C. Hu, et al., Chem. Eng. J. 431 (2022) 133930.
[84] Y. Cui, P. Yuan, W. Liu, et al., J. Mater. Chem. A 13 (2025) 3922–3934.
[85] Y. Cui, P. Yuan, F. Wang, et al., J. Alloy. Com. 980 (2024) 3922–3934.
[86] M. Zhang, S. Nie, T. Cheng, et al., Nano Energy 90 (2021) 106635.
[87] Z.L. Wang, Adv. Mater. 19 (2007) 889–892.
[88] J.A. Christman, R.R. Woolcott, A.I. Kingon, R.J. Nemanich, Appl. Phys. Lett. 73 (1998) 3851–3853.
[89] M.H. Zhao, Z.L. Wang, S.X. Mao, Nano Lett. 4 (2004) 587–590.
[90] N. Mahmood, H. Khan, K. Tran, et al., Mater. Today 44 (2021) 69–77.
[91] J.T. Luo, Y.C. Yang, X.Y. Zhu, et al., Phys. Rev. B 82 (2010) 014116.
[92] Y.C. Yang, C. Song, X.H. Wang, F. Zeng, F. Pan, J. Appl. Phys. 103 (2008) 074107.
[93] Y.C. Yang, C. Song, X.H. Wang, F. Zeng, F. Pan, Appl. Phys. Lett. 92 (2008) 012907.
[94] Y.J. Chen, S. Brahma, C.P. Liu, J.L. Huang, J. Alloy. Com. 728 (2017) 1248–1253.
[95] N. Sinha, G. Ray, S. Bhandari, S. Godara, B. Kumar, Ceram. Int. 40 (2014) 12337–12342.
[96] H. Yadav, N. Sinha, S. Goel, B. Kumar, J. Alloy. Com. 689 (2016) 333–341.
[97] S. Goel, N. Sinha, H. Yadav, et al., Mater. Chem. Phys. 202 (2017) 56–64.
[98] N. Sinha, S. Goel, A.J. Joseph, et al., Ceram. Int. 44 (2018) 8582–8590.
[99] Y. Huang, R. Fu, Z. Zhu, et al., ACS Appl. Mater. Interfaces 14 (2022) 39799–39807.
[100] Y. Wen, H. Che, C. Tang, B. Liu, Y. Ao, Nano Energy 128 (2024) 109795.
[101] D. Bhattacharya, S. Mukherjee, R.K. Mitra, S.K. Ray, Nanotechnology 34 (2023) 435401.
[102] C. Yu, X. Chen, C. Wang, Z. Wang, J. Phys. Chem. Solids 135 (2019) 109081.
[103] D. Günder, M. Axt, G. Witte, ACS Appl. Mater. Interfaces 16 (2023) 1911–1920.
[104] W. Wu, L. Wang, Y. Li, et al., Nature 514 (2014) 470–474.
[105] X. Wang, S. Liu, L. Huang, et al., Chem. Eng. J. 504 (2025) 159027.
[106] W. Choi, J. Kim, E. Lee, G. Mehta, V. Prasad, ACS Appl. Mater. Interfaces 13 (2021) 13596–13603.
[107] F. Meng, X. Luo, Y. Shi, et al., Colloids Surf. A: Physicochem. Eng. Asp. 693 (2024) 134096.
[108] S. Li, Z. Zhao, D. Yu, et al., Nano Energy 66 (2019) 104083.
[109] F. Meng, C. Guo, T. Cui, et al., Appl. Catal. B: Environ. 371 (2025) 125224.
[110] Z. Pan, W. Ding, H. Chen, H. Ji, Chin. Chem. Lett. 35 (2024) 108567.
[111] T. Ni, H. Zhang, L. Zhou, et al., Chin. Chem. Lett. 36 (2025) 110659.

[112] H. Zhao, Y. Ren, C. Liu, et al., J. Hazard. Mater. 459 (2023) 132117.
[113] Y. Ren, Y. Chu, N. Li, et al., Chem. Eng. J. 455 (2023) 140859.
[114] Y. Li, M. Gu, X. Zhang, et al., Mater. Today 41 (2020) 270–303.
[115] S. Chandratre, P. Sharma, Appl. Phys. Lett. 100 (2012) 023114.
[116] Z. Yu, Y. Li, A. Torres-Pinto, et al., Appl. Catal. B: Environ. 310 (2022) 121318.
[117] K. Wang, Z. Shu, J. Zhou, et al., J. Colloid Interf. Sci. 648 (2023) 242–250.
[118] C. Fu, T. Wu, G. Sun, et al., Appl. Catal. B: Environ. 323 (2023) 122196.
[119] C. Fu, M. Zhao, X. Chen, et al., Appl. Catal. B: Environ. 332 (2023) 122752.
[120] R. Tang, D. Gong, Y. Deng, et al., J. Hazard. Mater. 423 (2022) 126944.
[121] J. Wang, D. Liu, Y. Zhu, S. Zhou, S. Guan, Appl. Catal. B: Environ. 231 (2018) 251–261.
[122] R. Tang, D. Gong, Y. Zhou, et al., Appl. Catal. B: Environ. 303 (2022) 120929.
[123] G.D. Zhu, Z.G. Zeng, L. Zhang, X.J. Yan, Comp. Mater. Sci. 44 (2008) 224–229.
[124] E. Fukada, IEEE T. Ultrason, Ferr 47 (2000) 1277–1290.
[125] F. Meng, C. Liu, J. Guo, et al., Sep. Purif. Technol. 353 (2025) 128434.
[126] Y. Wang, Y.F. Wang, B.W. Hu, et al., Chem. Comm. 60 (2024) 7331–7334.
[127] W. Li, J. Tu, J. Sun, et al., Angew. Chem. Int. Ed. 64 (2024) e202413246.
[128] S. Huang, S. Yin, A. Kushwaha, et al., Chin. Chem. Lett. 37 (2026) 111211.
[129] H. Zhou, M.M. Baig, S. Gu, et al., Chin. Chem. Lett. 37 (2026) 111489.
[130] Y. Zhang, Y. Ren, J. Zhang, et al., Chem. Eng. J. 504 (2025) 158795.
[131] N. Stock, S. Biswas, Chem. Rev. 112 (2011) 933–969.
[132] J. Huang, H. Dong, L. An, M. Zhu, J. Qin, Chem. Eng. J. 504 (2025) 158555.
[133] D. Li, Q. Wen, C. Gao, et al., Chem. Eng. J. 498 (2024) 155079.
[134] I.M. Chirica, A.G. Mirea, Ş. Neaţu, et al., J. Mater. Chem. A 9 (2021) 19589–19612.
[135] M.S. Alam, M.A. Chowdhury, T. Khandaker, et al., RSC Adv. 14 (2024) 26995–27041.
[136] Y. Jia, K. Wang, C. Li, S. Liu, Mater. Today Sustain. 22 (2023) 100390.
[137] L. Jiang, C. Du, N. Xie, et al., J. Mol. Struct. 1321 (2025) 139928.
[138] H. Li, W. Ma, X. Zeng, et al., ACS Appl. Nano Mater. 6 (2023) 21113–21122.
[139] J. Peng, Y. He, C. Zhou, S. Su, B. Lai, Chin. Chem. Lett. 32 (2021) 1626–1636.
[140] G. Yin, C. Fu, F. Zhang, et al., J. Alloy. Com. 937 (2023) 168382.
[141] Q. Peng, H. Tian, H. Zhou, et al., Sep. Purif. Technol. 367 (2025) 132786.
[142] L. Wang, X. Huang, M. Han, et al., Appl. Catal. B: Environ. 257 (2019) 117904.
[143] S. Cheng, C. Zhang, X. Pan, et al., ACS Appl. Nano Mater. 5 (2022) 6832–6840.
[144] J. Yuan, X. Huang, L. Zhang, et al., Appl. Catal. B: Environ. 278 (2020) 119291.
[145] H. Lv, Y. Liu, J. Zhou, et al., Chem. Eng. J. 484 (2024) 149514.
[146] X. Zhou, X. Li, Y. Xiang, et al., Chin. Chem. Lett. 35 (2024) 110664.
[147] X. Dai, T. Liu, Y. Du, et al., Chin. Chem. Lett. 35 (2024) 110548.
[148] S. Sun, S. Song, S. Yang, et al., Chin. Chem. Lett. 35 (2024) 109242.
[149] X. Yang, F. Ye, Z. Li, et al., J. Environ. Chem. Eng. 12 (2024) 113013.
[150] H. Gao, Y. Zhang, H. Xia, et al., Dalton Trans. 51 (2022) 11876–11883.
[151] J. Xu, Q. Zhang, X. Gao, et al., Angew. Chem. Int. Ed. 62 (2023) e202307018.
[152] J. Xie, Q. Liu, L. Huang, et al., Chem. Eng. J. 487 (2024) 150685.
[153] T. Xu, L. Jin, Y. Ao, et al., Nat. Commun. 15 (2024) 10876.
[154] L. Chen, Z. Yang, J. Qian, B. Pan, Environ. Sci. Technol. 56 (2022) 14059–14068.
[155] H. Mei, Z. Gao, K. Zhao, et al., Angew. Chem. Int. Ed. 60 (2021) 21529–21535.
[156] Y. Chen, W. Ren, T. Ma, et al., Environ. Sci. Technol. 58 (2024) 4844–4851.
[157] R. Ghan, T. Shutava, A. Patel, V.T. John, Y. Lvov, Macromolecules 37 (2004) 4519–4524.
[158] Z. Chen, M. Xing, ACS Environ. Au 5 (2025) 148–151.
[159] Y.Q. Liu, L. Tian, M. Huang, et al., Environ. Sci. Technol. 59 (2024) 880–891.
[160] L. Peng, A. Yarman, K. Jetzschmann, et al., Sensors 16 (2016) 272.
[161] W. Ren, L. Xiong, G. Nie, et al., Environ. Sci. Technol. 54 (2019) 1267–1275.
[162] Z. Wang, X. Pan, L. Li, et al., Macromolecules 50 (2017) 7940–7948.
[163] C. Ding, Y. Yan, Y. Peng, et al., Macromolecules 55 (2022) 4056–4063.
[164] X. Chen, H. Xu, C. Liu, et al., Chem. Eng. J. 498 (2024) 155591.
[165] G. Singh, M. Sharma, R. Vaish, ACS Appl. Mater. Interfaces 13 (2021) 22914–22925.
[166] M. Xu, S. Yang, C. Guo, et al., Water Res. 283 (2025) 123865.
[167] J. Lei, C. Wang, X. Feng, et al., Chem. Eng. J. 435 (2022) 134624.
[168] A. Banerjee, A. Mukherjee, N. Bag, et al., J. Mol. Struct. 1298 (2024) 136996.
[169] Y.Q. Xie, Z.Q. Zhang, J. Wang, et al., Water Res. 284 (2025) 123977.